The Pennsylvania State University
The Graduate School

SIMILARITY MODELS OF SUBFILTER-SCALE ENERGY AND TEMPERATURE VARIANCE FOR LARGE EDDY SIMULATIONS OF THE ATMOSPHERIC BOUNDARY LAYER

A Thesis in
Meteorology
by
Scott Thomas Salesky

Submitted in Partial Fulfillment
of the Requirements
for the Degree of

Master of Science

August 2010

The thesis of Scott Thomas Salesky was reviewed and approved* by the following:

Marcelo Chamecki
Assistant Professor of Meteorology
Thesis Advisor

John C. Wyngaard
Professor Emeritus of Meteorology and Mechanical Engineering

Jose D. Fuentes
Professor of Meteorology

Johannes Verlinde
Professor of Meteorology
Associate Head, Graduate Program in Meteorology

*Signatures are on file in the Graduate School.

Abstract

Knowledge of the subfilter-scale (SFS) energy is instrumental for several reasons in Large Eddy Simulations (LES) of the atmospheric boundary layer (ABL). The SFS energy must be known to recover the true pressure field from the modified pressure used in simulations and may be used to form an eddy viscosity to model the SFS stress tensor. The SFS energy also must be known in LES of compressible flow to close the set of governing equations. The one-equation model, which determines the SFS energy through the numerical solution of its rate equation, is frequently used in LES. Although this approach is common, it has a high computational cost and requires closure assumptions. Several alternative models for the SFS energy have been proposed, including models formed by dimensional analysis, others that assume a spectral shape which is integrated to obtain the SFS energy, and others that are based on the hypothesis of scale similarity. Many of these models are strictly global, however, meaning that they can only predict the average SFS energy.

A local model is proposed for the SFS energy in LES of the ABL that is based on the scale similarity between the SFS energy and the trace of the Leonard stress tensor. The SFS energy model is derived from a stability-dependent atmospheric model of the energy spectrum that incorporates the effects of buoyancy and shear and therefore can account for the shape of the energy spectrum at low wavenumbers. Furthermore, this approach has a lower computational cost than the one-equation model, since the Leonard stress can be calculated easily in simulations.

Results from an *a priori* test using data from the Horizontal Array Turbulence Study (HATS) demonstrate that the model performs well in both a global and a local sense. The model is able to correctly predict the average SFS energy for most values of z/L and Δ/z considered, and does so more accurately than a similar model that assumes an infinite $\kappa^{-5/3}$ energy spectrum. The model also performs well in a local sense, producing a probability distribution function (PDF) similar to that of the actual SFS energy. This procedure is also extended to develop a model for the SFS temperature variance.

Table of Contents

List of Figures

List of Tables

List of Symbols

$\widetilde{(\cdot)}$	Filtered variable
c_I, c_{II}	Closure constants for spectral model
c_s	Smagorinsky coefficient
C_e	Kolmogorov constant for energy
C_θ	Kolmogorov constant for temperature
$D_e(z/L)$	Dissipative range function for model energy spectrum
$D_\theta(z/L)$	Dissipative range function for model temperature spectrum
e	Subfilter-scale energy
e_m	–5/3 model of subfilter-scale energy
e_{atm}	Atmospheric model of subfilter-scale energy
$E(\kappa)$	Energy spectrum
$E_\theta(\kappa)$	Temperature spectrum
$\mathrm{Erf}(z)$	Error function
$G(\boldsymbol{r})$	Filter kernel
$\widehat{G}(\kappa)$	Filter transfer function
k	von Kármán constant
ℓ_s	Smagorinsky lengthscale

L	Obukhov length
$\widetilde{L}_{ij}$	Leonard stress tensor
$\widetilde{L}_{\theta\theta}$	Leonard stress equivalent for temperature
p	Pressure
p^*	Modified pressure
$P(z/L)$	Production range function for spectral models
Pe_*	Friction velocity Péclet number
Re_*	Friction velocity Reynolds number
$\widetilde{S}_{ij}$	Filtered strain rate tensor
$\lvert\widetilde{S}\rvert$	Magnitude of strain rate tensor
u_i	Velocity vector
u_*	Friction velocity
z	Vertical coordinate
z_i	Atmospheric boundary layer depth
α	Mean wind angle
γ	Dissipative correction in SFS energy model of Knaepen et al. (2002)
δ_{ij}	Kronecker delta
$\bar{\Delta}$	Grid filter width
$\widetilde{\Delta}$	Test filter width
ε	Turbulent kinetic energy dissipation rate
η	Kolmogorov microscale
θ_*	Monin-Obukhov temperature scale
θ^2_{sfs}	Subfilter-scale temperature variance
θ^2_m	–5/3 model of subfilter-scale temperature variance

θ^2_{atm} Atmospheric model of subfilter-scale temperature variance

κ Wavenumber

κ_c Cutoff wavenumber

ν Kinematic viscosity

ν_r Eddy viscosity

ρ Density

τ_{ij} Subfilter-scale stress tensor

τ^m_{ij} Model of subfilter-scale stress tensor

ϕ_h Nondimensional temperature gradient

ϕ_m Nondimensional mean shear

ϕ_N Nondimensional destruction of temperature variance

ϕ_ϵ Nondimensional TKE dissipation rate

χ Thermal diffusivity

Acknowledgments

I am extremely grateful to Marcelo, for always taking the time to listen, for guidance around the many roadblocks that we encountered during the course of this research, for constructive criticism when I needed it, and for constant encouragement. I also would like the acknowledge my committee members, Jose Fuentes and John Wyngaard, for many thoughful suggestions on how to improve the quality and presentation of this research. I want to thank my parents, who have always told me that I could accomplish anything I set my mind to. I'm thankful to my friends who have put up with me during the last months while my head has been in the clouds. Finally, I'm thankful for the many outstanding science and math teachers in my life, most of whom have had a bigger impact on me than they may ever imagine. This thesis is dedicated to two of them in particular. First of all, to Gary Johnson, who taught me the meaning of hard work as a teacher, coach, and role model. Finally, this thesis is dedicated to Professor Marty Sponholz, for challenging me, for inspiring me, for sparking my curiousity, and for teaching excitement.

Chapter 1

Introduction

1.1 An Overview of Large Eddy Simulation

Fluid turbulence has long been recognized as an intractable mathematical problem due to the nonlinear nature of the Navier-Stokes equation, an elliptic partial differential equation which describes the momentum balance in a Newtonian fluid. By its very nature, turbulence is random, stochastic, and unpredictable. The understanding of turbulent flows is crucial not only for the advancement of scientific knowledge, but also for applied problems in fluid flow, heat transfer, and atmospheric dispersion.

Due to the analytical difficulties of approaching turbulence directly, research in turbulence has combined approximate theories with observations and laboratory experiments to gain a clearer understanding of the physics of fluid turbulence. As computational power has increased in the later half of the twentieth century, numerical modeling has become an attractive approach in obtaining information about turbulent flows.

Several distinct classes of numerical techniques, each with different purposes and advantages, have arisen to simulate turbulent flows. One of the most commonly used techniques for applied problems is Reynolds Averaged Navier-Stokes (RANS) modeling, which uses a closure model to account for the effects of the second moments and solves for the ensemble-mean velocity. While RANS has low computational cost, it is unable to provide information about the spectral distribution of turbulent quantities across a range of spatial or temporal scales since

only ensemble-mean quantities are calculated explicitly. On the opposite end of the modeling spectrum is Direct Numerical Simulation (DNS), which solves the Navier-Stokes exactly within numerical precision. While DNS resolves the entire range of scales in a turbulent flow down to the smallest dissipative eddies, it is limited to low or moderate Reynolds numbers due to its high computational expense. It is therefore used primarily as a research tool.

Large Eddy Simulation (LES) emerged as a viable method of modeling turbulent flows beginning with the work of Lilly (1967) and Deardorff (1970a; 1970b). LES is a compromise between RANS and DNS. By filtering the equations of motion and resolving only the large eddies, which carry fluxes of momentum, energy, and scalar constituents, LES reproduces a time-dependent realization of a turbulent flow with a reasonable computational cost. The effects of the smallest, dissipative eddies are represented in LES through a subfilter scale (SFS) model. LES has gained prominence both as a research tool and as an alternative to RANS that resolves a greater range of the turbulence directly in applied problems.

1.1.1 The Filtering Operation

The act of resolving only the large eddies in an LES can be viewed as applying a filter of width Δ to the governing equations. Motions at scales larger than Δ are explicitly resolved; scales smaller than Δ are represented by the SFS model. Although most filters in LES are implicit, since they are tied to the numerical discretization, the decomposition of a turbulent flow field into resolved and filtered components can be defined through a formal filtering operation (Leonard, 1974)

$$\tilde{f}(\boldsymbol{x}) = \int_{-\infty}^{+\infty} G(\boldsymbol{x} - \boldsymbol{x'}) f(\boldsymbol{x'}) d\boldsymbol{x'}. \tag{1.1}$$

Filtered variables are denoted by a tilde, and G is the filter function. The most commonly used filters in LES are the Box (1.2), Gaussian (1.3), and Spectral Cutoff (1.4) filters (Pope, 2000).

$$G(\boldsymbol{x} - \boldsymbol{x'}) = \frac{1}{\Delta} H\left(\frac{1}{2}\Delta - |\boldsymbol{x} - \boldsymbol{x'}|\right) \tag{1.2}$$

$$G(\boldsymbol{x}-\boldsymbol{x'}) = \left(\frac{6}{\pi\Delta^2}\right)^2 \exp\left(-\frac{6(\boldsymbol{x}-\boldsymbol{x'})^2}{\Delta^2}\right) \tag{1.3}$$

$$G(\boldsymbol{x}-\boldsymbol{x'}) = \frac{\sin(\pi(\boldsymbol{x}-\boldsymbol{x'})/\Delta)}{\pi(\boldsymbol{x}-\boldsymbol{x'})} \tag{1.4}$$

In (1.2), H denotes the Heaviside step function, which is defined as

$$H(x) = \begin{cases} 1 & x \geq 0 \\ 0 & x < 0. \end{cases} \tag{1.5}$$

The behavior of the filter in question must be taken into account when evaluating the performance of models. Since spectral analysis is such a useful tool in determining the behavior of a turbulent signal across a range of temporal and spatial scales, the effects of a given filter on the frequency or wavenumber domain must also be considered. In order to address this issue, it is useful to examine the properties of the transfer function (i.e. the Fourier transform of the filter function) associated with a given filter. The transfer functions for the Box, Gaussian, and Cutoff filters are given in (1.6)–(1.8) respectively, where $\kappa_c = \pi/\Delta$ is the cutoff wavenumber for the Spectral Cutoff Filter.

$$\widehat{G}(\kappa) = \frac{\sin(\frac{1}{2}\kappa\Delta)}{\frac{1}{2}\kappa\Delta} \tag{1.6}$$

$$\widehat{G}(\kappa) = \exp\left(-\frac{\kappa^2\Delta^2}{24}\right) \tag{1.7}$$

$$\widehat{G}(\kappa) = H(\kappa_c - |\kappa|) \tag{1.8}$$

While the Box Filter is positive definite in physical space, and can be simply viewed as a volume average over some region of the flow, its transfer function (1.6) is oscillatory in spectral space. Thus, the Box Filter retains some information about the behavior of the flow at high wavenumbers. Conversely, the transfer function of the Spectral Cutoff filter (1.8) is positive definite, but its filter function oscillates in physical space; therefore the Cutoff Filter eliminates high-wavenumber modes, but has nonlocal impacts on variables in physical space. The relative merits of

various filter types must be considered when choosing which filter to implement in a simulation.

After filtering, the momentum equation becomes

$$\frac{\partial \tilde{u}_i}{\partial t} + \tilde{u_j}\frac{\partial \tilde{u}_i}{\partial x_j} = -\frac{1}{\rho}\frac{\partial \tilde{p}}{\partial x_i} - 2\epsilon_{ijk}\Omega_j\widetilde{u}_k + \frac{\widetilde{\theta} - \Theta_0}{\Theta_0}g\delta_{3i} - \frac{\partial \tau_{ij}}{\partial x_j} \tag{1.9}$$

where the terms represent local change, advection, pressure gradient force, Coriolis force, buoyancy, and the divergence of the subfilter-scale (SFS) stress tensor respectively. The SFS tensor ($\tau_{ij} = \widetilde{u_i u_j} - \tilde{u}_i\tilde{u}_j$) arises through replacing a filtered product in the advective term ($u_j\frac{\partial u_i}{\partial x_j}$) with the product of filtered variables ($\widetilde{u}_j\frac{\partial \widetilde{u}_i}{\partial x_j}$) to retain the same physical character as the Navier-Stokes equation. τ_{ij} represents the effects of the dynamics of scales less than Δ and must be represented by a SFS model. The viscous term has been neglected in (1.9), since the resolved eddies have a high Reynolds number and therefore can be regarded as inviscid.

1.1.2 Subfilter-Scale Models

Since the resolved flow in LES is essentially inviscid for all filter widths encountered in typical applications, the divergence of the SFS stress tensor in (1.9) must serve as a surrogate for the viscous dissipation term in the Navier-Stokes equation. The primary purpose of the SFS model therefore is to remove energy from the resolved flow to account for the effects of the dissipative eddies that remain unresolved in LES. Desirable attributes of a SFS model include low computational cost, ease of implementation, Galilean invariance, and realizability[1] (Meneveau and Katz, 2000). The most common classes of SFS models will be reviewed briefly.

1.1.2.1 The Smagorinsky Model

The simplest model of the SFS stress, originally proposed by Smagorinsky (1963) for a general circulation model, relates the subfilter-scale stress tensor to the resolved rate of strain tensor through an eddy viscosity. The Smagorinsky model assumes that turbulent stress and strain have a linear relationship in a manner

[1]Realizability is satisfied if τ_{ij} is positive semi-definite. This condition is necessary to avoid nonphysical results, such as negative energy.

analogous to the relationship between molecular stress and strain given by the Stokes hypothesis. The Smagorinsky model is given as

$$\tau_{ij}^m - \frac{2}{3} e \delta_{ij} = -2\nu_r \widetilde{S}_{ij} \tag{1.10}$$

$$\nu_r = \ell_s^2 \left|\widetilde{S}\right| = (c_s \Delta)^2 \left|\widetilde{S}\right| \tag{1.11}$$

where τ_{ij}^m is used to denote a model of the SFS stress tensor, $e = \tau_{kk}/2$ is the subfilter scale energy, and $|\widetilde{S}| = (2\widetilde{S}_{ij}\widetilde{S}_{ij})^{1/2}$ is the magnitude of the strain rate tensor, defined as $\widetilde{S}_{ij} = (\widetilde{u}_{i,j} + \widetilde{u}_{j,i})/2$. ν_r denotes the eddy viscosity, ℓ_s is the Smagorinsky lengthscale, Δ is the filter width, and c_s is the Smagorinsky coefficient which can be adjusted to control the amount of energy transfered from the resolved scales to the subfilter-scales (Pope, 2000). The modeled stress tensor has only a deviatoric part since it is based on $\widetilde{S}_{ij}$ which is traceless. Although the Smagorinsky model is frequently criticized due to the low correlation coefficients between τ_{ij} and $\widetilde{S}_{ij}$, typically ranging from $0 - 0.25$ (Meneveau and Katz, 2000), and poor alignment between the eigenvectors of the two tensors (Higgins et al., 2003), it is used frequently in LES due to its robustness. When the Smagorinsky model for τ_{ij} is used, the divergence of the SFS stress in the filtered momentum equation (1.9) becomes similar in character to the viscous dissipation term in the Navier-Stokes and therefore is stable in numerical simulations. The Smagorinsky model is also popular due to its simplicity, low computational cost, and ease of implementation. It does not, however, allow for backscatter, the transfer of energy from subfilter to resolved scales that is observed in turbulent flows.

1.1.2.2 Similarity Models

Similarity models are based on the observation that the velocity field at a given spatial scale is closely influenced by motions at slightly larger scales. Similarity models exploit this principle by applying a test filter of width $\widetilde{\Delta}$ to resolved quantities that are calculated on a grid of width $\bar{\Delta}$. If τ_{ij} is defined using the filter of width $\bar{\Delta}$, an analogous quantity called the Leonard stress ($\widetilde{L}_{ij}$) can be defined by filtering a second time at a large scale where $\widetilde{L}_{ij} = \widetilde{\bar{u}_i \bar{u}_j} - \widetilde{\bar{u}}_i \widetilde{\bar{u}}_j$ following the Galilean-invariant decomposition given by Germano (1986). While τ_{ij} contains

information about scales close to $\bar{\Delta}$, $\widetilde{L}_{ij}$ is related to the velocity field at scales near $\widetilde{\Delta}$. The test filter $\widetilde{\Delta}$ is frequently taken to be twice the grid filter so that $\widetilde{L}_{ij}$ is defined in terms of scales close to $\bar{\Delta}$ where scale similarity is expected to hold.

The similarity model, originally proposed by Bardina et al. (1980), relates τ_{ij}^m to L_{ij} through a constant of proportionality

$$\tau_{ij}^m = C\widetilde{L}_{ij}. \tag{1.12}$$

Liu et al. (1994) found correlations between τ_{ij} and $\widetilde{L}_{ij}$ of $\rho = 0.4$–0.7 for the Box and Gaussian filters. However, when a Spectral Cutoff filter was used, τ_{ij} and $\widetilde{L}_{ij}$ were poorly correlated. Liu et al. attributed this result to the oscillatory nature of the Spectral Cutoff filter function in physical space, which eliminates correlation between local features of the flow. This result shows that one must be careful when using correlations to assess model performance, since they are dependent on filter type. Another advantage of the similarity model is a realistic representation of backscatter (Meneveau and Katz, 2000).

One drawback of the similarity model is that it does not dissipate enough energy to produce physical results in simulations (Meneveau and Katz, 2000). Bardina et al. (1980) proposed a mixed model that includes a contribution from $\widetilde{L}_{ij}$ to take advantage of the high correlations and realistic backscatter of the similarity model, and an eddy viscosity term to ensure that the modeled stress dissipates enough energy. The SFS stress is then modeled as

$$\tau_{ij}^m = C\widetilde{L}_{ij} - 2\nu_r\widetilde{S}_{ij}. \tag{1.13}$$

While the mixed model takes advantage of positive attributes of both similarity and eddy viscosity models, the model coefficients must be chosen to retain the correlations between τ_{ij} and $\widetilde{L}_{ij}$ while still dissipating enough energy from the resolved scales for the simulation to remain stable.

1.1.2.3 The Dynamic Model

In the traditional form of the Smagorinsky model, the model coefficient c_s must be specified empirically to ensure that the proper amount of energy is dissipated. If

too little energy is dissipated, an excess of energy will develop near scale Δ, leading to numerical instabilities; if too much energy is dissipated, the SFS model will extinguish the energy of the large eddies. However, the use of a single value of c_s can lead to inaccurate calculations in regions of the flow close to solid boundaries (Pope, 2000, p.599). The dynamic model, proposed by Germano et al. (1991), avoids the need to specify a coefficient explicitly by calculating c_s based on the resolved velocity field. The dynamic model therefore allows c_s to vary both in space and time and to take on different values throughout the flow. Germano et al. found

$$C = \frac{1}{2}\frac{L_{ij}\widetilde{S}_{ij}}{M_{ij}\widetilde{S}_{ij}} \tag{1.14}$$

where $M_{ij} = \widetilde{\Delta}^2|\widetilde{\bar{S}}|\widetilde{\bar{S}}_{ij} - \bar{\Delta}^2\widetilde{|\bar{S}|\bar{S}_{ij}}$, $\widetilde{\Delta}$ and $\bar{\Delta}$ denote the test and grid filters respectively, and C is the dynamic model coefficient. Lilly (1992) proposed solving for the coefficient in the least squares sense, where

$$C = \frac{1}{2}\frac{L_{ij}M_{ij}}{M_{ij}M_{ij}}. \tag{1.15}$$

The dynamic model has been found to predict the eddy viscosity in simulations better than the Smagorinsky model alone, but this may not necessarily improve simulation results due to numerical issues (Meneveau and Katz, 2000).

1.1.2.4 The Nonlinear Model

The nonlinear, or gradient model (Leonard, 1974; Clark et al., 1979; Liu et al., 1994), is based on the Taylor series expansion of the SFS stress. The stress is modeled as

$$\tau_{ij}^m = C\Delta^2\frac{\partial\tilde{u}_i}{\partial x_k}\frac{\partial\tilde{u}_j}{\partial x_k} \tag{1.16}$$

where C is a constant that depends on the filter type. The nonlinear model is only valid for the Box or Gaussian filters, as (1.16) is not defined for the Cutoff filter (Meneveau and Katz, 2000). While the nonlinear model has several advantages including high correlations, realistic backscatter, and correct alignment between the eigenvectors of the true and modeled stress (Lu and Porté-Agel, 2010), it does not dissipate enough energy in general. For this reason, the nonlinear model is

typically combined with a Smagorinsky component to create a mixed model.

An overview of additional models for the SFS stress and a more comprehensive treatment of those discussed here can be found in Mason (1994), Piomelli (1999), Meneveau and Katz (2000), and Sagaut (2006).

1.1.3 Tests of Model Performance

The most common classes of SFS models for large eddy simulation have been reviewed briefly in the previous section. While each model has certain advantages and disadvantages, one must define what it means for a model to perform well and consider how to best evaluate model performance. It clearly would be unrealistic to expect a model to reproduce the dynamics of the subfilter scales in a deterministic sense since turbulent fields fluctuate randomly in space and in time. However, we can hope for a model to perform well in a statistical sense, meaning that it predicts the mean and higher order moments of the velocity field accurately. In order to determine whether models meet these criteria, two common approaches to model evaluation have arisen: *a priori* and *a posteriori* tests. *A priori* tests decompose turbulence data into resolved and SFS components to directly compare τ_{ij} and τ_{ij}^m; *a posteriori* tests implement the model in an LES code and compare simulation output to experimental results for the same flow. It is important to recognize that the *a priori* and *a posteriori* approaches complement one another and together can provide information about different facets of model performance.

1.1.3.1 A Priori Tests

A priori tests decompose experimental turbulence data into resolved and SFS components to directly calculate τ_{ij} and τ_{ij}^m. Data for these tests may come from DNS, field or laboratory experiments, or high-resolution LES. The true and modeled stress tensors are calculated from the data, then their statistics are compared to quantify model performance. Mean values of τ_{ij} and τ_{ij}^m are commonly considered, but may not provide a comprehensive picture of model performance since two random variables may have the same mean but different probability distribution functions (PDFs). Correlation coefficients between the true and the modeled stress are another commonly considered statistic, but they also should be viewed with

some caution since correlations can depend on the type of filter used to decompose the velocity field into resolved and SFS parts (e.g. Liu et al., 1994). A fuller picture of the agreement between τ_{ij} and τ_{ij}^m can be provided by PDFs and joint PDFs which completely characterize the behavior of these two random variables. *A priori* tests have been conducted using DNS data of homogeneous turbulence (e.g. Clark et al., 1979; McMillan and Ferziger, 1979), laboratory measurements (e.g. Liu et al., 1994; Meneveau, 1994), and atmospheric boundary layer (ABL) data (e.g. Tong et al., 1999; Porté-Agel et al., 1998, 2000, 2001; Sullivan et al., 2003; Kleissl et al., 2003, 2004; Horst et al., 2004) using arrays of sonic anemometers to perform 2-D filtering, shown to be a good surrogate for the 3-D filter applied in LES (Horst et al., 2004). Array studies of ABL turbulence will be discussed in further detail in §4.1.

The principle motivation for using *a priori* tests for model evaluation is their direct calculation of τ_{ij}; this information is unavailable in LES. As a result, it is much easier to determine contributing factors to model performance than in the *a posteriori* case. One also avoids the computational expense of running simulations, perhaps repeatedly, to evaluate the model. However, *a priori* tests are unable to provide any information about how the model will actually perform in an LES code. Even if a model performs well in *a priori* tests, it may still experience numerical instabilities when implemented in LES.

1.1.3.2 A Posteriori Tests

A posteriori tests of model performance compare LES results to high-resolution turbulence data in order to determine whether the SFS model implemented in the LES code leads to correct predictions of the flow. Vreman et al. (1997) conducted an *a posteriori* analysis through comparison of LES output to filtered DNS data of a mixing layer. They considered the traditional forms of the Smagorinsky, similarity, and gradient models as well as dynamic models corresponding to each type of traditional model. In order to analyze model performance, Vreman et al. calculated total kinetic energy, rates of turbulent and molecular dissipation, backscatter of energy, magnitude of the SFS stress tensor components, energy spectrum evolution, vorticity, and momentum thickness. Each model was assigned a score (Table 2 in Vreman et al.) for each statistical category in order to quantify its agreement

with the DNS data. A similar analysis performed by Sarghini et al. (1999) focused on the scale-similar components of SFS models. They compared LES results to both DNS and experimental data for a two-dimensional plane channel flow and a three-dimensional boundary layer. In addition to intercomparing statistics for the various models, they also implemented each in an LES code to determine its computational expense.

While *a priori* tests can be instrumental in determining the statistical agreement between the true and modeled components of the SFS stress tensor, they provide little information about how a given model will perform in an actual simulation. For this reason, Meneveau and Katz (2000) call *a posteriori* tests the ultimate test of model performance, because they show conclusively whether a given SFS model will correctly predict the evolution of the flow. Furthermore, *a posteriori* tests are necessary to determine the computational expense and numerical stability of a model when implemented in an LES code.

However, diagnostic variables calculated from DNS or experimental data are not always identical to their counterparts from large eddy simulation. For example, the Reynolds stresses calculated from experimental data may differ from the *filtered Reynolds stresses* obtained from LES (Pope, 2000). The agreement between the two quantities is a function of Δ/ℓ, the ratio of filter width to integral scale in the LES. Though comparison of LES results with DNS or experimental data can give conclusive evidence of model performance, it may be difficult to determine why a model performs as it does using an *a posteriori* analysis alone.

1.2 Motivation for Modeling SFS Energy and Temperature Variance

In order for the Smagorinsky model to have the same dimensions as the true stress, the eddy viscosity must have units of $\nu_r = [L]^2\,[T]^{-1}$. One may form the eddy viscosity in the traditional form of the Smagorinsky model, given in (1.10)–(1.11), using $\ell_s = c_s\,\Delta$ as a lengthscale and $|\widetilde{S}|^{-1}$ as a timescale. However, since the SFS energy has units of $e = [L]^2\,[T]^{-2}$, an alternative definition of the eddy viscosity is

possible

$$\nu_r = c_k \, \Delta \, e^{1/2} \tag{1.17}$$

where c_k is a model coefficient distinct from c_s. Using the SFS energy to prescribe a timescale has certain advantages. Piomelli (1999) argues that using an eddy viscosity based on the energy should lead to a more accurate prediction of the SFS timescale, since the information contained in $|\widetilde{S}|$ is biased toward larger-scale structures of the flow. One would expect this to be the case since $|\widetilde{S}|$ is based only on resolved scale quantities and would therefore be expected to contain information about the velocity field at or near scale Δ. However, the SFS energy is defined in terms of quantities that occur at spatial scales less than Δ, which implies that eddy viscosity models based on e contain inherently more information about subfilter-scale dynamics.

The SFS energy must also be known in LES to obtain the pressure field, a key diagnostic variable in ABL flows. Since most models for τ_{ij} are based on $\widetilde{S}_{ij}$, which is strictly deviatoric, the SFS stress is decomposed in the deviatoric and isotropic components, i.e. $\tau_{ij} = \tau_{ij}^d + \frac{2}{3} \, e \, \delta_{ij}$ where the deviatoric part of τ_{ij} is denoted by τ_{ij}^d and the isotropic part of τ_{ij} is related to the SFS energy. The isotropic part of τ_{ij} is then included in a modified pressure: $\widetilde{p}^* = \widetilde{p}/\rho + \frac{2}{3} \, e$. For LES of incompressible flow, the modified pressure is found through the solution of the Poisson equation

$$\nabla^2 \widetilde{p}^* = -\frac{\partial \widetilde{u}_i}{\partial x_j} \frac{\partial \widetilde{u}_j}{\partial x_i} - \frac{\partial^2 \tau_{ij}^d}{\partial x_i \partial x_j} \tag{1.18}$$

that is obtained through taking the divergence of the filtered momentum equation (1.9). To obtain the true pressure field from this modified pressure, however, the SFS energy must be known.

Another motivation for modeling the SFS energy occurs in the LES of compressible turbulent flows, where the divergence of the velocity field cannot be assumed to be identically zero. In this case, (1.18) is no longer valid. An evolution equation for the true pressure can be derived from the full compressible continuity equation and the equation of state, but an equation for the modified pressure that is calculated in LES only may be obtained if the SFS energy is known. A model of the SFS energy is therefore necessary to complete the LES equation set for compressible turbulent flows.

The question then is how to attain e, which is an unknown quantity in LES. The traditional approach (e.g. Schumann, 1975; Deardorff, 1980; Moeng, 1984) has been to solve the evolution equation for e (2.1) under certain closure assumptions. Eddy viscosity models that follow this procedure are known as one-equation models. However, the computational expense of solving the energy rate equation numerically is quite high. It therefore is desirable to model e so that information about the subfilter scales can be accounted for in an eddy viscosity while minimizing the computational expense. A review of existing SFS energy models can be found in §2.1. A model for e that accounts for atmospheric parameters is derived in §3.3.1; its performance is analyzed in §5.1.

While developing and assessing a model for the SFS energy is the main focus of this work, our analysis can be easily extended to model the variance of a passive scalar. We chose to model θ_{sfs}^2, the SFS temperature variance, because sonic virtual temperature data is part of the Horizontal Array Turbulence Study (HATS) dataset (e.g. Tong et al., 1999; Porté-Agel et al., 1998, 2000, 2001; Sullivan et al., 2003; Kleissl et al., 2003, 2004; Horst et al., 2004), which we are using to evaluate our model in an *a priori* test. The temperature variance is a measure of the inhomogeneity of the temperature field; a model for the subfilter scale component allows one to reconstruct the full variance if the resolved temperature field is known. Furthermore, having information available about θ_{sfs}^2 has modeling implications since it appears in the evolution equation for the SFS heat flux. While we chose to develop and evaluate a model of the SFS temperature variance, one just as easily could apply our procedure to model to any arbitrary passive scalar such as concentration of a chemical species or water vapor mixing ratio. This model therefore has broader implications for LES, where our procedure can be applied to reconstruct the total scalar variance σ_c^2. Furthermore, the ratio between $\langle \widetilde{L}_{\alpha\alpha} \rangle$ (no sum on α) and $\langle \widetilde{L}_{ii} \rangle$ can be used to split the SFS energy into its components to estimate the SFS part of σ_u^2, σ_v^2, and σ_w^2, the variances of the three velocity components.

Chapter 2

Review of the Literature

2.1 Models of SFS Energy

The SFS energy can be obtained through the numerical solution of its rate equation as in one-equation models, or through models that are designed to account for its basic physical properties. Sagaut (2006) recognizes three main categories of SFS energy models, each of which will be considered: models formed by dimensional analysis, which depend on the filter width and magnitude of the strain rate, similarity models, which relate e to $\widetilde{L}_{ii}$, and dissipation-based models, which are based on the integration of the energy spectrum. One-equation models will be reviewed briefly, followed by a discussion of each class of model proposed by Sagaut.

2.1.1 Models Based on the SFS Energy Rate Equation

The full evolution equation for the SFS energy is

$$\begin{aligned}\frac{\partial e}{\partial t} + \widetilde{u}_k \frac{\partial e}{\partial x_k} = \\ -\frac{1}{2}\frac{\partial}{\partial x_k}\left[\widetilde{u_i u_i u_k} - 2\widetilde{u}_i\widetilde{u_i u_k} - \widetilde{u}_k\widetilde{u_i u_i} + 2\widetilde{u}_i\widetilde{u}_i\widetilde{u}_k\right] - \frac{1}{\rho}\frac{\partial}{\partial x_k}\left[\widetilde{p u_k} - \widetilde{p}\,\widetilde{u}_k\right] \\ +\nu\frac{\partial^2 e}{\partial x_k \partial x_k} - \nu\left[\widetilde{\frac{\partial u_i}{\partial x_k}\frac{\partial u_i}{\partial x_k}} - \frac{\partial \widetilde{u}_i}{\partial x_k}\frac{\partial \widetilde{u}_i}{\partial x_k}\right] - \frac{1}{2}\tau_{ik}\left[\frac{\partial \widetilde{u}_i}{\partial x_k} + \frac{\partial \widetilde{u}_k}{\partial x_i}\right]\end{aligned} \tag{2.1}$$

where the terms represent local change, advection, triple correlation, pressure transport, viscous diffusion, viscous dissipation, and production of SFS energy

by the resolved scales respectively.

One-equation models solve (2.1) numerically after modeling the triple correlation, pressure transport, and viscous dissipation terms, which are unknown. This type of approach was used by Schumann (1975) to develop a subfilter-scale model for finite difference models of turbulent flow in plane channels and annuli. Ghosal et al. (1995) and Carati et al. (1995) solved the evolution equation for e to determine an eddy viscosity in localized dynamic models. One-equation models also have been used for large eddy simulations of atmospheric boundary layer flows. Deardorff (1980) used this approach to simulate the mixed boundary layer containing stratocumulus. Moeng (1984) implemented a one-equation model in a pseudospectral code for the LES of ABL turbulence. Shaw and Schumann (1992) solved an evolution equation for e that incorporated canopy drag in an LES of flow within a forest.

Although one-equation models are common in LES, closure assumptions must be made to model the unknown terms in (2.1). Direct solution of the SFS energy equation also has a higher computational expense than other methods. Piomelli (1999) argues that the improvement in accuracy of using e to specify a velocity scale for an eddy viscosity model over the traditional approach is not justified by the added computational cost. SFS energy models have been developed in order to take advantage of the improvement in accuracy by using a SFS velocity scale based on $e^{1/2}$ while minimizing the increase in computational expense.

2.1.2 Models Formed by Dimensional Analysis

Yoshizawa (1986) proposed a model for the SFS energy based on dimensional analysis. The SFS energy (actually energy per unit mass) has units of $e = [L]^2\,[T]^{-2}$, where L is length and T is time. Yoshizawa proposed using a lengthscale proportional to Δ and a timescale proportional to $|\widetilde{S}|^{-1}$ as in the Smagorinsky model to obtain

$$e_m = 2C\Delta^2|\widetilde{S}|^2 \tag{2.2}$$

where C is a proportionality constant. Moin et al. (1991) used Yoshizawa's model for the energy to develop a subgrid model for compressible turbulence. They evaluated C dynamically using the Germano identity. Wong and Lilly (1994)

followed a similar procedure as Yoshizawa (1986) to develop a subgrid model for turbulent thermal convection.

While dimensional models for the energy have a low computational expense and are straightforward to implement in a simulation, it is important to recognize that basing an eddy viscosity on (2.2) does not introduce new information beyond what is already present in the Smagorinsky model, since e_m depends on Δ and $|\widetilde{S}|$. One can show that the Smagorinsky model reduces to the traditional form with different constants if the eddy viscosity is formulated as $\nu_r = C\,\Delta\,e^{1/2}$ and (2.2) is used to model the energy. The dimensional energy model is expected to to yield a similar prediction of the SFS timescale as the traditional Smagorinsky model; therefore, it is not expected to be as accurate as other methods.

2.1.3 Similarity Models

A similarity-type model has been proposed by Knaepen et al. (2002), where the SFS energy is taken to be proportional to the energy contained in the scales between $\widetilde{\Delta}$ and $\bar{\Delta}$, where $\widetilde{\Delta}$ is the test filter scale and $\bar{\Delta}$ is the grid filter scale. The model can be written as $e_m = C\widetilde{L}_{ii}$, where C is a constant of proportionality. An expression for this constant may be derived analytically by assuming that the energy has a Kolmogorov spectrum and $\widetilde{\Delta}$ and $\bar{\Delta}$ lie in the inertial subrange. Integration of the energy spectrum yields a constant that is a function of the grid and test filter widths and depends on the filter type. Knaepen et al. also added a correction to account for the effects of the dissipative range of the energy spectrum. This similarity model has a relatively low computational expense, since $\widetilde{L}_{ij}$ is easily obtainable in most LES codes. A more detailed discussion of the assumptions underlying the Knaepen et al. model, its derivation, and a discussion of its performance can be found in §3.1.

2.1.4 Dissipation Based Models

Models of the SFS energy can also be formulated through integration of the energy spectrum (Misra and Pullin, 1997; Voelkl et al., 2000; Pullin, 2000)

$$e = \int_o^\infty (1 - \widehat{G}(\kappa)^2) E(\kappa) d\,\kappa \tag{2.3}$$

where $\widehat{G}(\kappa)$ is the filter transfer function. If the Spectral Cutoff filter is used, (2.3) reduces to

$$e = \int_{\kappa_c}^{\infty} E(\kappa) d\kappa \tag{2.4}$$

where κ_c is the cutoff wavenumber. Since $E(\kappa)$ depends on ε, the rate of viscous dissipation of turbulent kinetic energy, Sagaut (2006) refers to this class of models as dissipation-based models. In order to derive this type of SFS energy model, one must assume a shape for the energy spectrum and evaluate the integral in (2.3) for a given filter type. This approach has been used by Misra and Pullin (1997) to develop a model of the SFS stress based on the vorticity. They assumed the energy spectrum to take the shape of

$$E(\kappa) = \begin{cases} C_e \varepsilon^{2/3} \kappa^{-5/3}, & \kappa_c \leq \kappa \leq J\kappa_\eta \\ 0, & \kappa > J\kappa_\eta \end{cases} \tag{2.5}$$

where $\kappa_\eta = 1/\eta$ is the wavenumber associated with the Kolmogorov microscale $\eta = (\nu^3/\varepsilon)^{1/4}$, and J is a cutoff parameter. Both Misra and Pullin (1997) and Pullin (2000) argue for the use of $J = 1$ so that the energy decays near the Kolmogorov microscale. Although this model simplifies the effects of the dissipation range, Misra and Pullin argue that its performance is adequate for LES modeling efforts, since only the cumulative effect of the subgrid scales is of interest. The total dissipation rate is assumed to be the sum of dissipation from the resolved scales and the subfilter scales

$$\varepsilon = 2\nu \widetilde{S}_{ij} \widetilde{S}_{ij} + \varepsilon_{sfs}. \tag{2.6}$$

Using a cutoff filter that is assumed to lie in the inertial subrange, then SFS dissipation and the transfer of energy from the resolved to the subfilter scale can be equated

$$\varepsilon_{sfs} = -\tau_{ij} \widetilde{S}_{ij}. \tag{2.7}$$

Upon carrying out the integration in (2.4), the model for the energy is (Pullin, 2000)

$$e_m = \begin{cases} \frac{3C_e \varepsilon^{2/3}}{2\kappa_c^{2/3}} \left(1 - \left(\frac{\kappa_c}{\kappa_\eta} \right)^{2/3} \right), & \kappa_c \leq \kappa \leq J\kappa_\eta \\ 0, & \kappa > J\kappa_\eta. \end{cases} \tag{2.8}$$

The model requires the simultaneous solution of a system of nonlinear equations, since e_m depends on $\tau_{ij}\widetilde{S}_{ij}$ through the dissipation rate, but τ_{ij} depends on e_m through the eddy viscosity coefficient. Pullin (2000) used the model energy spectrum in (2.5) to develop a SFS model for the flux of a passive scalar based on vorticity.

The vorticity-based subgrid stress model of Misra and Pullin (1997) was extended to physical space using structure functions by Voelkl et al. (2000). They obtained

$$e_m = \tfrac{3}{2} C_e \varepsilon^{2/3} \kappa_c^{-2/3} \tag{2.9}$$

as a model for the energy, where $C_e\varepsilon^{2/3}$ is estimated on a local basis (eq. 20 in Voelkl et al.) through a function of the average of the second order structure function that corresponds to the model energy spectrum given in (2.5).

Meyers and Baelmans (2004) propose another dissipation-based model for the SFS energy based on the integration of an energy spectrum that contains a low wavenumber damping function

$$e_m = \int_{\bar{\kappa}_c}^{\infty} C_e \varepsilon^{2/3} \kappa^{-5/3} F(\kappa L) d\,\kappa \tag{2.10}$$

where $\bar{\kappa}_c = \pi/\Delta$ is the filter wavenumber and L is the integral lengthscale. The choice of nondimensional function $F(\kappa L)$ is restricted by consistency relations that require realistic behavior for the energy, enstrophy ($\mathcal{E} = \frac{1}{2}\langle \vec{\omega} \cdot \vec{\omega} \rangle$, where $\vec{\omega}$ is the vorticity vector), and palinstrophy ($\mathcal{P} = \frac{1}{2}\langle (\vec{\nabla} \times \vec{\omega})^2 \rangle$). While the above model is intended to give an *a priori* estimate of the SFS energy for model setup purposes, Meyers and Baelmans propose an additional SFS energy model for implementation in LES. However, this extended model is not evaluated directly.

Dissipation-based models for the SFS energy have lower computational cost than solving the SFS energy evolution equation (2.1) directly. They assume a functional form for $E(\kappa)$ and estimate the SFS energy through integrating the energy spectrum over all wavenumbers beyond the cutoff. It is difficult to assess how accurately this class of models performs since these models have not been evaluated directly by Misra and Pullin (1997), Voelkl et al. (2000), Pullin (2000), or Meyers and Baelmans (2004). Furthermore, these models are strictly global, meaning they can only predict the mean SFS energy.

2.2 Models of SFS Temperature Variance

As Sagaut (2006) points out, virtually any model for the SFS energy can be extended to the SFS temperature variance. A similarity model for the SFS variance of an arbitrary conserved scalar was proposed by Cook and Riley (1994). Pierce and Moin (1998) proposed a dynamic model where the variance of an arbitrary Favre filtered passive scalar was modeled as

$$\widetilde{\rho\phi''^2} = C\Delta^2\tilde{\rho}|\nabla\tilde{\phi}|^2 \tag{2.11}$$

and the coefficient C was evaluated using the dynamic procedure.

In general, the modeling of SFS scalar variance has not received as much attention as the SFS energy. However, several distinct types of models have been proposed for general subgrid scalar quantities. One class of models is based on deconvolution, where the SFS scalar variance is calculated by applying the inverse of the filtering operator to the filtered scalar field (Sagaut, 2006). The constants that arise in deconvolution-type models can be evaluated dynamically (Sagaut, 2006), or calculated by matching the moments of the filtered scalar field to an arbitrary order following the approach of Pantano and Sarkar (2001). Sagaut also points out that θ^2_{sfs} may be found through the numerical solution of its evolution equation as with the energy, or by assuming a form for the temperature spectrum and evaluating an expression similar to 2.3.

Chapter 3

Similarity Models of Subfilter-Scale Energy and Temperature Variance

A model for the SFS energy, based on the scale similarity between $\widetilde{L}_{ii}$ and e was proposed by Knaepen et al. (2002). Their model has certain advantages over the one-equation model including lower computational cost and ease of implementation. The similarity model of Knaepen et al. will be reviewed briefly. Models of the energy and temperature spectra in the atmospheric surface layer proposed by Claussen (1985a) will then be reviewed and used to develop atmospheric models for the SFS energy and temperature variance.

3.1 Review of a Similarity Model for SFS Energy

3.1.1 Derivation of the Model

The SFS energy model proposed by Knaepen et al. (2002) requires applying a test filter of width $\widetilde{\Delta}$ to the velocity field in order to calculate $\widetilde{L}_{ij}$. Both filters are assumed to lie in the inertial subrange. In general, the SFS energy can be found by evaluating the integral

$$\langle e \rangle = \int_0^\infty (1 - \widehat{\overline{G}}(\kappa)^2) E(\kappa) d\,\kappa \tag{3.1}$$

and the energy contained in scales between $\widetilde{\Delta}$ and $\bar{\Delta}$ can be found from

$$\langle \widetilde{L}_{ii} \rangle = 2 \int_0^\infty (\widehat{\overline{G}}(\kappa)^2 - \widehat{\widetilde{G}}(\kappa)^2) E(\kappa) d\,\kappa \tag{3.2}$$

where $\widehat{\overline{G}}(\kappa)$ is the transfer function of the grid filter and $\widehat{\widetilde{G}}(\kappa)$ is the transfer function of the test filter. If one assumes that a spectral cutoff filter is used as Knaepen et al. did in their derivation, equations (3.1) and (3.2) reduce to

$$\langle e \rangle = \int_{\bar{\kappa_c}}^\infty E(\kappa) d\kappa \tag{3.3}$$

and

$$\langle \widetilde{L}_{ii} \rangle = 2 \int_{\widetilde{\kappa}_c}^{\bar{\kappa_c}} E(\kappa) d\kappa \tag{3.4}$$

where $\bar{\kappa}_c = \pi/\bar{\Delta}$ and $\widetilde{\kappa}_c = \pi/\widetilde{\Delta}$ denote the wavenumbers of the grid and test filters.

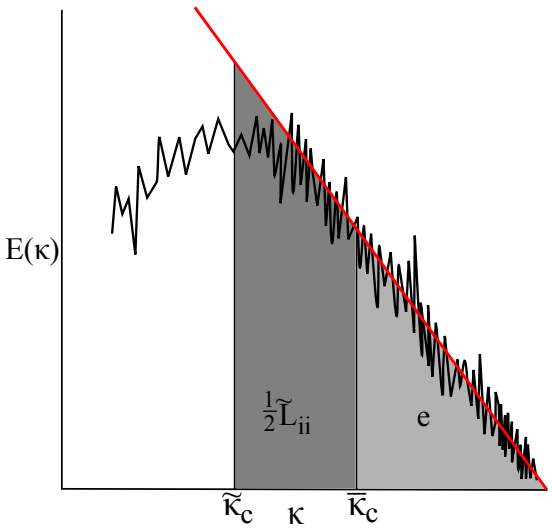

Figure 3.1. A schematic drawing of –5/3 energy model, based on Knaepen et al. (2002). Here the energy spectrum $E(\kappa)$, which integrates to the total turbulent kinetic energy, is plotted as a function of wavenumber (κ) and the locations of the Leonard stress ($\widetilde{L}_{ii}/2$), the SFS energy (e), the test filter wavenumber ($\widetilde{\kappa}_c$), and the grid filter wavenumber ($\bar{\kappa}_c$) are displayed. The black line is the typical shape of a calculated atmospheric energy spectrum; the red line is the –5/3 line used to derive the model.

Figure 3.1 shows the relationship of the test and grid filters to the Leonard

stress in the energy spectrum when a cutoff filter is used. Since Knaepen et al. (2002) assumed that both $\widetilde{\kappa_c}$ and $\bar{\kappa_c}$ lie in the inertial subrange, the energy spectrum is given by $E(\kappa) = A_1\kappa^{-5/3}$, where $A_1 = C_e\varepsilon^{2/3}$. Instead of estimating ε, A_1 is determined using information from $\langle\widetilde{L}_{ii}\rangle$. Substituting $E(\kappa)$ into (3.4) and evaluating the integral yields

$$A_1 = \frac{\langle\widetilde{L}_{ii}\rangle}{3\left[\widetilde{\kappa_c}^{-2/3} - \bar{\kappa_c}^{-2/3}\right]}. \tag{3.5}$$

The value of A_1 from (3.5) is then substituted into $E(\kappa)$ and (3.3) is evaluated which gives the following model for the SFS energy:

$$e_m = \frac{\widetilde{L}_{ii}}{2\left[\left(\frac{\tilde{\Delta}}{\bar{\Delta}}\right)^{2/3} - 1\right]} \tag{3.6}$$

where e and $\widetilde{L}_{ii}$ are written without the brackets because we will later consider the performance of (3.6) in a local sense.

Since Knaepen et al. (2002) assessed model performance in an *a priori* test using DNS data, they also calculated a correction to account for the effects of the dissipative range of the energy spectrum. The energy model then becomes

$$e_m = \frac{\widetilde{L}_{ii}}{2\left[\left(\frac{\tilde{\Delta}}{\bar{\Delta}}\right)^{2/3} - 1\right]}(1 - \gamma^{2/3}) \tag{3.7}$$

where $\gamma = \bar{\kappa_c}/\widetilde{\kappa}_{\tilde{\epsilon}}$ is the correction factor, and

$$\widetilde{\kappa}_{\tilde{\epsilon}} = \left(\bar{\kappa_c}^{4/3} - \frac{2\langle\tau_{ij}\widetilde{S}_{ij}\rangle}{3\nu A_1}\right)^{3/4} \tag{3.8}$$

is an estimate of the wavenumber where dissipative effects begin to dominate. Due to the wide range of spatial scales at typical Reynolds numbers encountered in the ABL, it is reasonable to assume $\widetilde{\kappa}_{\tilde{\epsilon}} \gg \bar{\kappa}_c$, which implies $\gamma \ll 1$. Results from our data analysis indicate that this correction factor is indeed negligible for ABL flows.

3.1.2 Model Performance

Knaepen et al. (2002) analyzed the model in an *a priori* test to a 512^3 DNS database of decaying isotropic turbulence. They found that the model with the dissipative correction (3.7) was able to accurately predict the temporal evolution of the global SFS energy. It performed better than both the model without the correction (3.6) and the dimensional SFS energy model given by Yoshizawa (1986). However, they cautioned against extending the model to estimate e on a local basis. While the PDFs of e and e_m exhibited reasonable agreement at the first timestep, correlation coefficients were found to be very low (3.0×10^{-2}). We shall further evaluate the Knaepen et al. model using atmospheric data and intercompare its performance with our atmospheric model.

The model proposed by Knaepen et al. will be further evaluated using atmospheric data in §5 and its performance will be compared with that of the atmospheric model proposed in §3.3.1.

3.1.3 Extension to the Temperature Variance

While not explicitly addressed by Knaepen et al., a similar analysis can be used to derive a model for the subfilter-scale temperature variance, defined as $\theta_{sfs}^2 = \overline{\theta\theta} - \bar{\theta}\bar{\theta}$. If a cutoff filter is assumed, the SFS temperature variance can be found through integration of the temperature spectrum over all wavenumbers beyond the cutoff

$$\langle \theta_{sfs}^2 \rangle = \int_{\bar{\kappa}_c}^{\infty} E_\theta(\kappa)\, d\kappa. \tag{3.9}$$

The equivalent of the Leonard stress for the temperature, $\widetilde{L}_{\theta\theta} = \widetilde{\bar{\theta}\bar{\theta}} - \tilde{\bar{\theta}}\tilde{\bar{\theta}}$, can be found by integrating $E_\theta(\kappa)$ between the test and grid filter wavenumbers

$$\langle \widetilde{L}_{\theta\theta} \rangle = \int_{\tilde{\kappa}_c}^{\bar{\kappa}_c} E_\theta(\kappa)\, d\kappa. \tag{3.10}$$

A similar procedure to that given above for the energy yields the following model of the SFS temperature variance:

$$\theta_m^2 = \frac{\widetilde{L}_{\theta\theta}}{\left[\left(\frac{\widetilde{\Delta}}{\bar{\Delta}}\right)^{2/3} - 1\right]}. \tag{3.11}$$

Results of *a priori* tests of model performance are given in §5.2.

3.2 Models of Atmospheric Energy and Temperature Spectra

The similarity model of the SFS energy proposed by Knaepen et al. (2002) is valid for filters that lie in the inertial subrange of turbulence. In LES of the ABL, however, the first several grid points near the surface necessarily have a filter width that is similar to the integral scale of turbulence (e.g. Mason, 1994; Sullivan et al., 2003; Kleissl et al., 2004; Chamecki, 2010). As a result, it is especially important to account for the behavior of the production range of the energy spectrum, which depends on buoyancy and mean shear, when $\Delta \gtrsim z$. We introduce the effects of buoyancy and shear into our model by replacing the Kolmogorov spectrum with the model for the energy spectrum in the atmosphere given by Claussen (1985a). The exponential damping function that accounts for low-wavenumber behavior in this spectral model loosens the restriction that $\bar{\kappa}_c$ and $\widetilde{\kappa}_c$ both lie in the inertial subrange. Since the same procedure will be followed to model the SFS temperature variance, Claussen's model of the temperature spectrum will also be introduced here.

3.2.1 Derivation

Claussen derives the models for the energy and temperature spectra under the assumptions of stationarity and horizontal homogeneity. The spectral energy and temperature budget equations, given as functions of height and wavenumber, are

$$-M(z,\kappa)\frac{d\bar{U}}{dz} + H(z,\kappa)\frac{g}{\Theta_0} + T_{we}(z,\kappa) + T_e(z,\kappa) - 2\nu\kappa^2 E(z,\kappa) = 0 \qquad (3.12)$$

$$-H(z,\kappa)\frac{d\bar{\Theta}}{dz} + T_{w\theta}(z,\kappa) + T_\theta(z,\kappa) - 2\chi\kappa^2 E_\theta(z,\kappa) = 0. \qquad (3.13)$$

Equation (3.12) is the dynamic equation for the energy spectrum, where the terms represent mechanical production, buoyant production/destruction, combined pressure and turbulence transport, nonlinear spectral energy transfer, and viscous dissipation, respectively. The terms in equation (3.13), the dynamic equation for the temperature spectrum, represent mean gradient production, turbulent transport of temperature variance, nonlinear transfer of variance, and molecular destruction of temperature variance, respectively.

In (3.12) and (3.13), $E(z,\kappa)$ is the turbulent kinetic energy spectrum, $E_\theta(z,\kappa)$ is the turbulent temperature spectrum, $M(z,\kappa)$ is the spectral momentum flux, $H(z,\kappa)$ is the spectral temperature flux, $T_{we}(z,\kappa)$ is a nonlinear spectral transfer due to turbulence-turbulence interactions and the velocity-pressure covariance, $T_e(z,\kappa)$ is the divergence of a spectral energy flux, $T_{w\theta}(z,\kappa)$ is the spectral vertical transport of temperature variance, and $T_\theta(z,\kappa)$ is the nonlinear spectral transfer of temperature variance, where ν is the kinematic viscosity and χ is the thermal diffusivity.

In order to solve (3.12) and (3.13) for the energy and temperature spectra, the transfer and mean gradient production terms must be modeled in order to close the equations. Claussen models the nonlinear transfer terms by forming the divergence of a spectral energy flux dimensionally. The mean gradient production term is written as an unknown function of two characteristic timescales through Buckingham's Pi Theorem and then linearized. A local timescale is then formed dimensionally from the inverse of the mean velocity gradient to model this unknown function.

Claussen gives models for the energy and temperature spectra under unstable, neutral, and stable conditions that require use of two closure constants, c_I and c_{II}. Claussen gives the relationship between the constants as being proportional to the relationship between the nondimensional mean shear and temperature gradient as

a function of z/L

$$\frac{c_{II}}{c_I} = c_{IV}\frac{\phi_m}{\phi_h} \tag{3.14}$$

where c_{IV} is a multiplicative constant which we take to be equal to 1. The following models of the energy and temperature spectra, given in their dimensional form, are found upon applying Claussen's closure hypotheses to solve (3.12) and (3.13) and using the relationship (3.14) between the constants[1]

$$E(z,\kappa) = C_e\,\varepsilon^{2/3}\kappa^{-5/3}\exp[-P\,\kappa^{-4/3}]\exp[-D_e\,\kappa^{4/3}] \tag{3.15}$$

$$E_\theta(z,\kappa) = C_\theta\,\varepsilon^{-1/3}N\kappa^{-5/3}\exp[-P\,\kappa^{-4/3}]\exp[-D_\theta\,\kappa^{4/3}]. \tag{3.16}$$

C_e and C_θ are the Kolmogorov constants for the energy and temperature spectra respectively; N is the rate of molecular dissipation of temperature variance. The functions within the exponentials, which control the behavior of the spectra within the production range (3.17) and dissipation range (3.18) and (3.19) are

$$P(z/L) = \frac{3}{4}C_e(c_I\phi_m^2 - c_{II}\frac{z}{L}\phi_h)\phi_\epsilon^{-2/3}(kz)^{-4/3} \tag{3.17}$$

$$D_e(z/L) = \frac{3}{2}C_e Re_*^{-1}\phi_\epsilon^{-1/3}(kz)^{4/3} \tag{3.18}$$

$$D_\theta(z/L) = \frac{3}{2}C_\theta Pe_*^{-1}\phi_N^{-1/3}(kz)^{4/3}. \tag{3.19}$$

In (3.17)–(3.19), $L = -\frac{u_*^3\Theta_0}{kg(\overline{w'\theta'})_0}$ is the Obukhov length, where Θ_0 is a reference temperature and $(\overline{w'\theta'})_0$ is the surface heat flux, $Re_* = \frac{kzu_*}{\nu}$ is the friction velocity Reynolds number, $Pe_* = \frac{kzu_*}{\chi}$ is the friction velocity Péclet number, and $k = 0.4$ is the von Kármán constant. A value of $c_I = 0.15$ was used in our analysis, following Dias and Brutsaert (1998); c_{II} was determined from (3.14) where we take $c_{IV} = 1$. While the resultant models for the energy and temperature spectra given in (3.15) and (3.16) are similar to Claussen's stable model, the models used here are more general because the ratio c_{II}/c_I is a function of z/L rather than being constant as in the stable Claussen model.

In equations (3.17)–(3.19), ϕ_h, ϕ_m, ϕ_N, and ϕ_ϵ are respectively the nondi-

[1]Several typographical errors appear in the equations in the original paper by Claussen (1985a). We believe the expressions given in (3.15)–(3.19) are the correct ones.

mensional mean temperature gradient, mean shear, destruction of temperature variance, and viscous dissipation of TKE predicted by Monin-Obukhov similarity theory (MOST), defined as

$$\phi_h = \frac{kz}{\theta_*}\frac{\partial \bar{\Theta}}{\partial z} \tag{3.20}$$

$$\phi_m = \frac{kz}{u_*}\frac{\partial \bar{U}}{\partial z} \tag{3.21}$$

$$\phi_N = \frac{kzN}{u_*\theta_*^2} \tag{3.22}$$

$$\phi_\epsilon = \frac{kz\varepsilon}{u_*^3}. \tag{3.23}$$

where θ_* is the Monin-Obukhov temperature scale, and N is the rate of molecular destruction of temperature variance.

Since the total energy, $E = (\sigma_u^2 + \sigma_v^2 + \sigma_w^2)/2$, is the sum of the variances of the three velocity components, the energy spectrum contains contributions from the spectra of u, v, and w. While the peak wavenumber of the vertical velocity spectrum (Λ_w) scales with z in the atmospheric surface layer, thus following MOST, the peak wavenumbers of the horizontal velocity components (Λ_u and Λ_w) scale with the boundary layer depth z_i (Kaimal and Finnigan, 1994, p.43). A model energy spectrum therefore should depend on both z/L and z/z_i. This fact is not accounted for by Claussen, who models the energy spectrum as a function of κ and z/L only. The production range of the spectrum is controlled by an exponential damping function. However, this behavior is different from the κ^{-1} behavior that has been observed at low wavenumbers in the atmosphere (Katul et al., 1995), which also is not accounted for by Claussen.

3.2.2 Agreement with Calculated Atmospheric Spectra

Claussen also derives models for the energy and temperature spectra under neutral and stable stratification. When the normalized nondimensional spectra are plotted for $-1.0 \leq z/L \leq 2.0$, the spectral peaks shift to higher wavenumbers with increasing stability. The amplitude of the peak of the energy spectrum decreases steadily as z/L increases. The same general trend is also present in the temperature spectrum, although it exhibits bimodal behavior for near-neutral stratification.

In a companion paper (Claussen, 1985b), the spectral models are used to predict the nondimensional ϕ functions of MOST. Claussen used the measured nondimensional peak wavenumbers from the Kansas experiment (Kaimal et al., 1972) to estimate ϕ_m and ϕ_h from the spectral models. Estimates of ϕ_m from the Kansas data exhibit reasonable agreement with the empirical predictions of Dyer (1974) for $-1.0 \leq z/L \leq 1.0$; the estimate of ϕ_h fits the empirical curve well for $-2.0 \leq z/L \leq 1.0$. The models of the energy and temperature spectra therefore appear to perform reasonably well for $-1.0 \leq z/L \leq 1.0$, although the absence of a κ^{-1} region in the spectra is an inherent limitation.

3.3 Proposed SFS Models for Atmospheric Turbulence

The Claussen models for the energy and temperature spectra are used to derive similarity models for SFS energy and temperature variance following the methodology of Knaepen et al. (2002). The resultant models for e and θ_{sfs}^2 depend on z/L through the MOST functions, and Δ/z through $\widetilde{L}_{ii}$.

3.3.1 Energy

The expressions given in (3.1) and (3.2) are general enough to extend to any arbitrary filter function $\widehat{G}(\kappa)$ and any form chosen for the energy spectrum $E(\kappa)$. To be rigorous, the SFS energy model should be derived by substituting the Claussen energy spectrum (3.15) and the transfer function for the filter used in our analysis into (3.2) to determine a coefficient for the energy spectrum, then evaluating (3.1) with this coefficient to derive a model for the SFS energy. However, it is difficult to give an exact form for the filter transfer function that we used. The data were filtered with a Box Filter in the x-direction and the timeseries was resampled to width $\bar{\Delta}$ following the procedure described in §4.2. While the transfer function for the Box Filter is given in (1.6), the transfer function associated with the resampling operation is unknown. Furthermore, this approach yields integrals that cannot be calculated in closed form. If a Cutoff Filter is assumed, however, one may derive an analytical expression for the SFS energy model. We found in our analysis that

using the transfer function of the Box Filter and evaluating the resultant integrals numerically did not offer a significant improvement over the analytical expression for the SFS energy derived below, where a Cutoff Filter is assumed.

To derive a model for the SFS energy that depends on atmospheric parameters, we again note that if a Cutoff Filter is used, $\langle \widetilde{L}_{ii} \rangle$ is twice the energy spectrum integrated from the test wavenumber to the grid wavenumber as in (3.4).

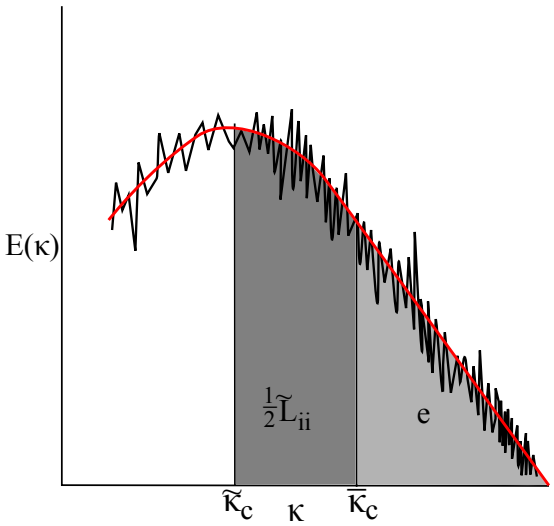

Figure 3.2. A schematic drawing of the proposed atmospheric energy model. Here the energy spectrum $E(\kappa)$, which integrates to the total turbulent kinetic energy, is plotted as a function of wavenumber (κ) and the locations of the Leonard stress ($\widetilde{L}_{ii}/2$), the SFS energy (e), the test filter wavenumber ($\widetilde{\kappa}_c$), and the grid filter wavenumber ($\bar{\kappa}_c$) are displayed. The black line is the typical shape of a calculated atmospheric energy spectrum; the red line is the model energy spectrum given by Claussen which accounts for the shape of the production range of the spectrum.

In order to account for the effects of buoyancy and shear, we substitute the Claussen model for $E(\kappa)$ (3.15) in the place of the Kolmogorov spectrum. A schematic drawing of how the Claussen model accounts for the shape of the production range of the spectrum is given in Figure 3.2. Notice that when $\widetilde{\kappa}_c$ does not lie in the inertial subrange, $\langle \widetilde{L}_{ii} \rangle/2$ still is equal to the integrated energy spectrum between $\widetilde{\kappa}_c$ and $\bar{\kappa}_c$, which is not true of the –5/3 energy spectrum displayed in Figure 3.1. The exponential function that controls the dissipative range in (3.15) is neglected, which allows us to evaluate (3.24) analytically. Denoting the constant

of proportionality by A_2, we have

$$\langle \widetilde{L}_{ii} \rangle = 2 \int_{\widetilde{\kappa}_c}^{\bar{\kappa}_c} A_2 \, \kappa^{-5/3} \exp[-P\kappa^{-4/3}] d\kappa \tag{3.24}$$

The integration was performed in Mathematica; upon solving for A_2, one finds

$$A_2 = \frac{2\langle \widetilde{L}_{ii} \rangle \sqrt{P}}{3\sqrt{\pi} \left[\mathrm{Erf}\left(\frac{\sqrt{P}}{\widetilde{\kappa}_c^{2/3}} \right) - \mathrm{Erf}\left(\frac{\sqrt{P}}{\bar{\kappa}_c^{2/3}} \right) \right]} \tag{3.25}$$

where $\mathrm{Erf}(z) = \frac{2}{\sqrt{\pi}} \int_0^z e^{-t^2} dt$ is the error function. The model for the SFS energy can be found by substituting A_2 into (3.26) and integrating

$$\langle e_m \rangle = \int_{\bar{\kappa}_c}^{\infty} A_2 \, \kappa^{-5/3} \exp[-P\kappa^{-4/3}] d\kappa. \tag{3.26}$$

The resultant model for the SFS energy is

$$e_m = \frac{\widetilde{L}_{ii}}{2 \left[\dfrac{\mathrm{Erf}\left(\frac{\sqrt{P}}{\widetilde{\kappa}_c^{2/3}} \right)}{\mathrm{Erf}\left(\frac{\sqrt{P}}{\bar{\kappa}_c^{2/3}} \right)} - 1 \right]} \tag{3.27}$$

where the effects of buoyancy and shear are accounted for through $P(z/L)$ (3.17). The performance of (3.27) is evaluated in §5 in an *a priori* test using HATS data.

3.3.2 Temperature Variance

The same procedure can be applied to obtain a model for the SFS temperature variance, $\theta_{sfs}^2 \equiv \overline{\theta\theta} - \bar{\theta}\bar{\theta}$. We begin by defining the equivalent of the Leonard stress for temperature $\widetilde{L}_{\theta\theta} = \widetilde{\bar{\theta}\bar{\theta}} - \tilde{\bar{\theta}}\tilde{\bar{\theta}}$ and noting that it is equal to the integral of the temperature spectrum between the test filter and grid filter wavenumbers:

$$\langle \widetilde{L}_{\theta\theta} \rangle = \int_{\widetilde{\kappa}_c}^{\bar{\kappa}_c} E_\theta(\kappa) \, d\kappa \tag{3.28}$$

Here we use the Claussen model for the temperature spectrum (3.16), neglecting the exponential that controls the dissipative range for the same reason as with the

energy, and denote the unknown coefficient as A_3

$$\langle \widetilde{L}_{\theta\theta} \rangle = \int_{\widetilde{\kappa}_c}^{\bar{\kappa}_c} A_3 \, \kappa^{-5/3} \exp[-P\kappa^{-4/3}] d\kappa \tag{3.29}$$

Upon evaluating the integral in (3.29) and solving for the unknown coefficient A_3, one obtains

$$A_3 = \frac{4\langle \widetilde{L}_{\theta\theta} \rangle \sqrt{P}}{3\sqrt{\pi} \left[\mathrm{Erf}\left(\frac{\sqrt{P}}{\widetilde{\kappa}_c^{2/3}} \right) - \mathrm{Erf}\left(\frac{\sqrt{P}}{\bar{\kappa}_c^{2/3}} \right) \right]}. \tag{3.30}$$

The temperature spectrum is integrated for all wavenumbers beyond $\bar{\kappa}_c$ to obtain the following model for the SFS temperature variance

$$\theta_m^2 = \frac{\widetilde{L}_{\theta\theta}}{\left[\dfrac{\mathrm{Erf}\left(\frac{\sqrt{P}}{\widetilde{\kappa}_c^{2/3}} \right)}{\mathrm{Erf}\left(\frac{\sqrt{P}}{\bar{\kappa}_c^{2/3}} \right)} - 1 \right]}. \tag{3.31}$$

Chapter 4

Methodology

The models of SFS energy and temperature variance were evaluated in an *a priori* test to atmospheric data from the Horizontal Array Turbulence Study experiment (e.g. Tong et al., 1999; Porté-Agel et al., 1998, 2000, 2001; Sullivan et al., 2003; Kleissl et al., 2003, 2004; Horst et al., 2004). The HATS experiment is briefly reviewed, together with an overview of the data analysis procedure. Rationale is also given for resampling the data after filtering.

4.1 The HATS Dataset

Although SFS models are often evaluated through direct comparisons to filtered DNS data, this approach is limited to low to moderate Reynolds numbers due to the computational expense of DNS.[1] In order to conduct *a priori* tests at higher Reynolds numbers, atmospheric data is an attractive alternative. Some of the first field experiments to use horizontal arrays of sonic anemometers, which allow for 2-D spatial filtering, were conducted by Tong et al. (1999) and Porté-Agel et al. (2000, 2001). Turbulence data can be filtered with a discrete filter in the crosswind direction and through Taylor's hypothesis in the streamwise direction, which allows one to interpret timeseries measurements as spatial data. Sonic anemometers are deployed in a double array in the vertical so that vertical gradients of resolved quantities can be estimated through a finite-difference approximation. The 2-D

[1] The number of Fourier modes required in a DNS to resolve all of the scales of motion increases exponentially with the Reynolds number, i.e. $N^3 \sim Re^{9/4}$ (Pope, 2000).

filter serves as a surrogate for the 3-D filters that are typically implemented in LES. This filter is used to decompose experimental data into resolved and SFS components so that SFS quantities may be calculated directly in an *a priori* test.

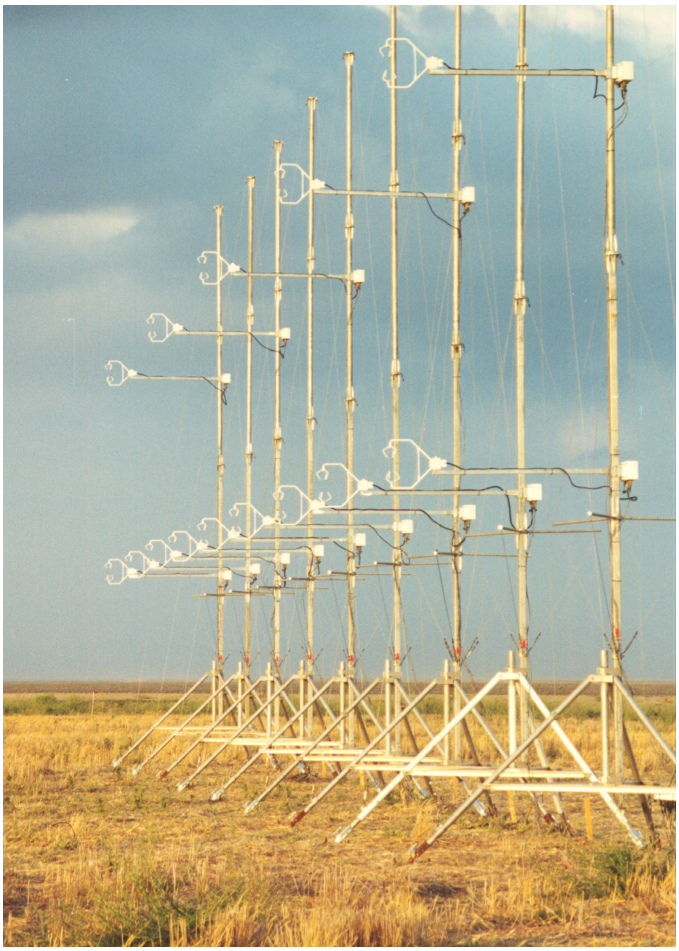

Figure 4.1. A photograph of the HATS array configuration.

The Horizontal Array Turbulence Study (HATS) was conducted near Kettleman City, CA in late 2000. One of the goals of HATS was to collect data over a wider range of atmospheric stabilities (z/L) and ratios of filter width to vertical integral scale of turbulence (Δ/z) than previous studies (Horst et al., 2004).

A double array of 14 sonic anemometers was deployed in 4 separate configurations during the course of the experiment. We considered data from Arrays 1, 2, and 3 in our analysis; characteristics of these arrays are given in Table 4.1. Arrays 1 and 2 have 9 sonics in the lower ("double") array and 5 sonics in the

Array	z (m)	δy (m)	δz (m)	Δ (m)	Δ/z
1	3.45	3.35	3.45	6.70	2.0
2	4.33	2.17	4.33	4.33	1.0
3	4.33	1.08	4.33	2.17	0.5

Table 4.1. HATS arrays used to evaluate SFS models. z is height of the lower array, δy is the horizontal distance between the sonics on the lower array, δz is the vertical distance between the sonics, $\Delta = 2\delta y$ is the filter width, and Δ/z is the ratio of filter width to integral scale.

upper ("single") array. In Array 3, the single and double arrays are inverted so that the double array is on top. Further details of the HATS experiment and array geometries can be found in Kleissl et al. (2003) and Horst et al. (2004).

4.2 Data Analysis Procedure

The data analysis was performed using Fortran 90 code. The HATS data were split into 27.3 minute blocks to calculate statistics, equivalent to 32768 points per block sampled at 20 Hz. Before filtering, the array of anemometers was aligned so that the mean wind was perpendicular to the array (i.e. $\bar{V} = 0$) following the procedure given in Kaimal and Finnigan (1994, p.236).

In order to align the array, the average horizontal unrotated components of the velocity vector (u_1 and v_1) were calculated. The wind angle was then calculated via

$$\alpha = \tan^{-1}\left(\frac{u_1}{v_1}\right). \tag{4.1}$$

The rotated components of the velocity vector (u_2 and v_2) are related to the unrotated components by

$$u_2 = u_1 \cos\alpha + v_1 \sin\alpha \tag{4.2}$$

$$v_2 = -u_1 \sin\alpha + v_1 \cos\alpha \tag{4.3}$$

In order to limit the amount of corrections applied to the data during rotation, only blocks with $|\alpha| \leq 45°$ were included in the analysis. After rotation, it is also necessary to align the points in the timeseries of each sonic to correct for the time lag that is introduced. The sonics are aligned following the procedure of Kleissl

et al. (2003), where $u_i^{aligned}(x, y, z, t) = u_i(x, y, z, t - \delta y \sin\alpha / \langle u \rangle)$.

The data were filtered using a 2-D box filter with a width of $\bar{\Delta} = 2\,\delta y$ in both the crosswind and the streamwise directions to decompose the velocity field into resolved and SFS components. The effective filter width after rotation is related to the the unrotated filter by $\bar{\Delta}_{eff} = \bar{\Delta}\cos\alpha$ (Kleissl et al., 2003). The widths of the unrotated filters are given in Table 4.1. Double-filtered quantities (e.g. $\widetilde{L}_{ij}$ and $\widetilde{L}_{\theta\theta}$) were calculated using a double filter width of $\widetilde{\Delta} = 2\,\bar{\Delta} = 4\,\delta y$. $\widetilde{\Delta}$ and $\bar{\Delta}$ will subsequently be used to denote the effective filter widths.

It is important to recognize that the results of an *a priori* analysis can depend on the type of filter used. For example, higher correlations between resolved and subfilter-scale variables are typically found using a Box Filter than a Spectral Cutoff Filter, since the transfer function of the Box Filter (1.6) is not positive definite in Fourier space and therefore retains a contribution from wavenumbers greater than the filter wavenumber. Liu et al. (1994) found correlations between τ_{ij} and $\widetilde{L}_{ij}$ of $\rho = 0.5$–0.7 when a Box Filter was used, values of $\rho = 0.4$–0.6 for a Gaussian Filter, but negligible ($\rho < 0.1$) correlations with a Spectral Cutoff Filter for sufficiently small Δ/η. They attributed the difference between filter types to the oscillatory nature of the Spectral Cutoff Filter function (1.4) in physical space, which leads to the loss of correlation on local scales.

To limit the influence of small scale information when assessing model performance, the data are resampled following the procedure of Liu et al. (1994) so that τ_{ij} is calculated using only information that would be available in LES (i.e. on a grid of width $\bar{\Delta}$). When the data are filtered in the x-direction using Taylor's hypothesis, the timeseries is resampled so that points in the new series have a spacing of $\bar{\Delta}$. The double-filtered variables must similarly be resampled at width $\widetilde{\Delta}$. The shorter series that results from the resampling procedure is then used to calculate statistics including average values of e and e_m and PDFs. When the data are resampled after filtering, only a small portion of the original series is used. In order to obtain better statistical convergence, the code loops through all possible subsets of points that can be used to obtain a resampled series. Statistics for each of these subsets are then averaged to obtain a single value of each statistic for the 27.3 minute block.

We used the following forms of the MOST functions given by Kaimal and

Finnigan (1994, p.16) in our calculations of e_m and θ_m^2

$$\phi_m = \begin{cases} (1 + 16\,|z/L|)^{-1/4}, & -2 \le z/L \le 0 \\ (1 + 5\,z/L), & 0 \le z/L \le 1 \end{cases} \tag{4.4}$$

$$\phi_h = \begin{cases} (1 + 16\,|z/L|)^{-1/2}, & -2 \le z/L \le 0 \\ (1 + 5\,z/L), & 0 \le z/L \le 1 \end{cases} \tag{4.5}$$

$$\phi_\epsilon = \begin{cases} (1 + 0.5\,|z/L|^{2/3})^{3/2}, & -2 \le z/L \le 0 \\ (1 + 5\,z/L), & 0 \le z/L \le 1 \end{cases}. \tag{4.6}$$

The forms of the ϕ functions given by Kaimal and Finnigan are based on the results of the Kansas experiment (Wyngaard and Coté, 1971), with some corrections based on more recent observations. We also calculated e_m and θ_m^2 using the forms of the ϕ functions given by Högström (1988), but found that this had negligible impact on our results.

Chapter 5

Performance of Models

We conducted an *a priori* test using the HATS dataset in order to assess the performance of the atmospheric SFS energy and temperature variance models. Results indicate that the atmospheric models improve significantly upon the model of Knaepen et al. for neutral and stable conditions and perform well in a local sense under most conditions. We analyzed model performance using average values, PDFs, and joint PDFs. Average values demonstrate how the models perform in a global sense; PDFs and JPDFs indicate how models perform in a local sense. The agreement between the true and modeled energy and temperature variance depends on the ratio of filter width to vertical integral scale of turbulence (Δ/z) and stability (z/L). Data from three HATS array configurations allow us to consider Δ/z values of 2.0, 1.0 and 0.5. The HATS data were collected over a wide range of atmospheric stabilities, which allows us to determine the z/L dependence of our models. We limited our analysis to $-1 \leq z/L \leq 1$, however, for several reasons. First, little data exists for the most unstable conditions (i.e. $z/L < -1$). Secondly, the universal ϕ functions predicted by MOST are only defined between -2 and 1 in most studies (e.g. Foken, 2006). Finally, while the HATS dataset contains data for $z/L > 1$, we do not attempt to extend our analysis to these stabilities due to the difficulty associated with modeling the stable atmospheric boundary layer. The stability criteria that is used in this analysis is given in Table 5.1.

Stability	z/L Range
Very Unstable	$-1.00 \leq z/L \leq -0.50$
Moderately Unstable	$-0.50 \leq z/L \leq -0.03$
Neutral	$-0.03 \leq z/L \leq 0.03$
Moderately Stable	$0.03 \leq z/L \leq 0.50$
Very Stable	$0.50 \leq z/L \leq 1.00$

Table 5.1. Stability criteria used to determine z/L dependence of the models.

5.1 SFS Energy Model

5.1.1 Global Performance

For a SFS energy model to perform well in a global sense, it must predict the average SFS energy accurately. We tested global model performance by comparing the average values of e and e_m for each block of data. Figure 5.1 is a scatterplot of the average SFS energy predicted by two SFS energy models plotted against the true energy. The top panel is the model of Knaepen et al. (3.6), which we shall refer to as the "–5/3 model." The bottom panel contains the proposed atmospheric model of the SFS energy (3.27). One datapoint is plotted for each 27.3 minute block following the filtering and resampling procedure describe in §4.2. Separate markers are used for each values of Δ/z, and stable cases (i.e. $z/L > 0.5$) are plotted separately. Here e, e_m, and e_{atm} denote the true SFS energy, the –5/3 model, and the atmospheric model respectively.

The results shown in Figure 5.1 indicate that the –5/3 model of the energy has a clear Δ/z dependence. The model systematically underpredicts the true energy for $\Delta/z = 2.0$ and 1.0; agreement between e and e_m improves as Δ/z decreases. This can be attributed to the assumption that both the single and double filter lie in the inertial subrange, which is not necessarily true for larger Δ/z. With the exception of several very stable cases where $\Delta/z = 2.0$, the atmospheric model predicts the true energy accurately for all values of z/L and Δ/z that were tested. This improvement over the –5/3 model can be attributed to the production range correction in Claussen's spectral model. Since $P(z/L)$ accounts for the shape of the spectrum at low wavenumbers, it is not necessary for the single and double filters to lie in the inertial subrange for the model to predict the average correctly.

To examine how global model performance depends on stability, the averages predicted by the models are normalized by $\langle e \rangle$ and plotted against z/L in Figure 5.2. While the –5/3 model yields accurate predictions of the average under unstable and neutral conditions for small Δ/z, its accuracy decreases with increasing stability. The agreement between $\langle e \rangle$ and $\langle e_m \rangle$ once again improves as Δ/z decreases. The atmospheric model exhibits less scatter than the –5/3 model, especially for the neutral and unstable cases. With a filter width of $\Delta/z = 2.0$, the atmospheric model begins overpredicting the true energy as stability exceeds $z/L > 0.5$. The atmospheric model predicts $\langle e \rangle$ more accurately for stable conditions, however, as the filter width decreases.

5.1.2 Local Performance

Average values calculated from the HATS data indicate that the atmospheric energy model predicts the average SFS energy accurately under all conditions except for the most stable cases when $\Delta/z = 2.0$. However, the correct prediction of the average is not a conclusive measure of model performance. Two random variables could have the same mean but low correlation coefficients and different probability distribution functions.

We found correlation coefficients between e and e_m of approximately 0.3–0.5 for $\Delta/z = 2.0$, 0.4–0.6 for $\Delta/z = 1.0$, and near 0.7 for $\Delta/z = 0.5$. Our results are similar to the correlations that Liu et al. (1994) found between the diagonal components of τ_{ij} and $\widetilde{L}_{ij}$ in the far field of a round jet calculated using a box filter. We expect that these correlations would be lower for a Gaussian or Spectral Cutoff filter. While the correlation coefficients calculated in our analysis are similar to those of Liu et al. (1994), it is important to recognize that correlation coefficients have significant shortcomings in determining model performance. A pair of random variables may be highly correlated, but have different averages and PDFs. The PDFs and joint PDFs of a pair of random variables provide a more complete characterization of their behavior and therefore are used here to quantify local model performance.

Probability distribution functions were calculated for the true and modeled energy normalized by σ_e, the standard deviation of the true SFS energy. PDFs

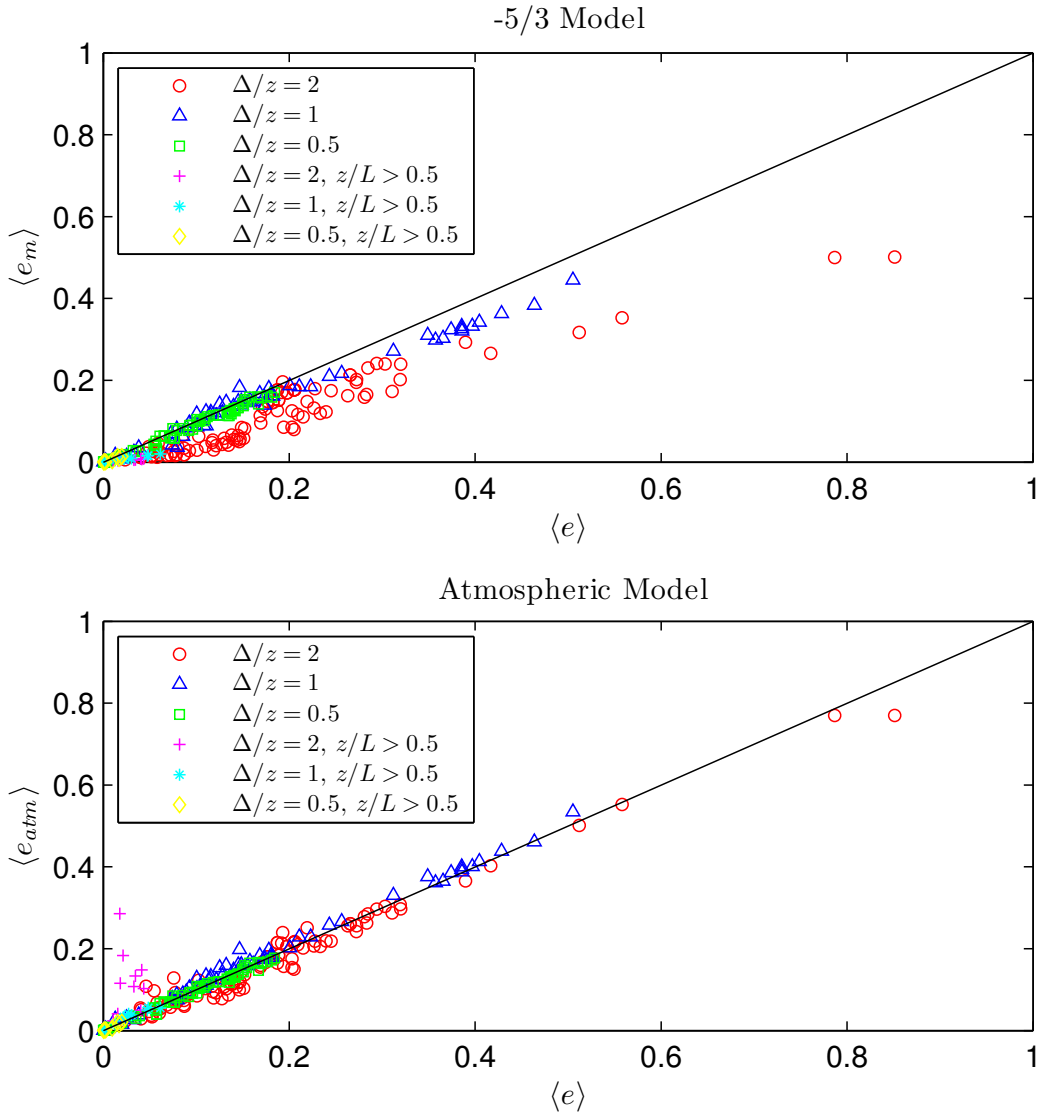

Figure 5.1. Scatterplots of the average values of the true and modeled SFS energy for each 27.3 minute block of data.

were calculated for each block of data, then averaged across all blocks of similar stability following the criteria given in Table 5.1. PDFs for $\Delta/z = 2.0$, 1.0, and 0.5 are displayed in Figures 5.3, 5.4, and 5.5, respectively.

For the very unstable runs, both the –5/3 and the atmospheric model have similar PDFs for all filter widths. For $\Delta/z = 2.0$ and 1.0 in moderately unstable and neutral cases, the atmospheric model predicts the distribution of the true

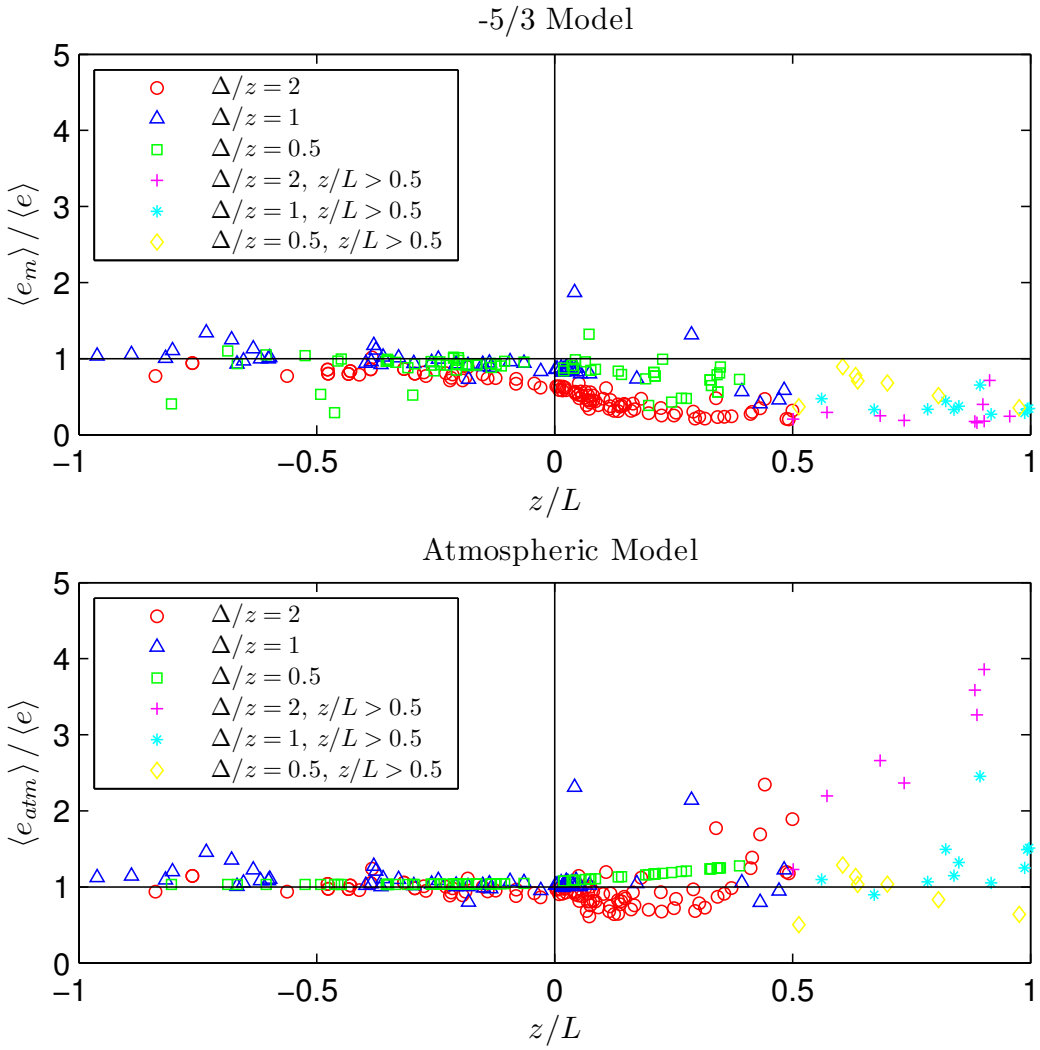

Figure 5.2. Ratios of the average modeled energy to the true SFS energy as a function of z/L.

energy better than the –5/3 model. The difference between the two models becomes particularly pronounced in the moderately stable and very stable cases where the difference between predictions made by the two models increases. As was evident from the plots of the averages (Figures 5.1 and 5.2), the atmospheric model predicts the true energy poorly for the very stable cases when $\Delta/z = 2.0$.

The predictions made by the two models converge for $\Delta/z = 0.5$, so if one were to use a small enough filter in LES, the –5/3 model could be used to obtain similar results as the atmospheric model. The atmospheric model therefore predicts the

PDF of the true energy more accurately than the –5/3 model for larger filter widths ($\Delta/z = 2.0$ and 1.0) and under neutral or stable conditions.

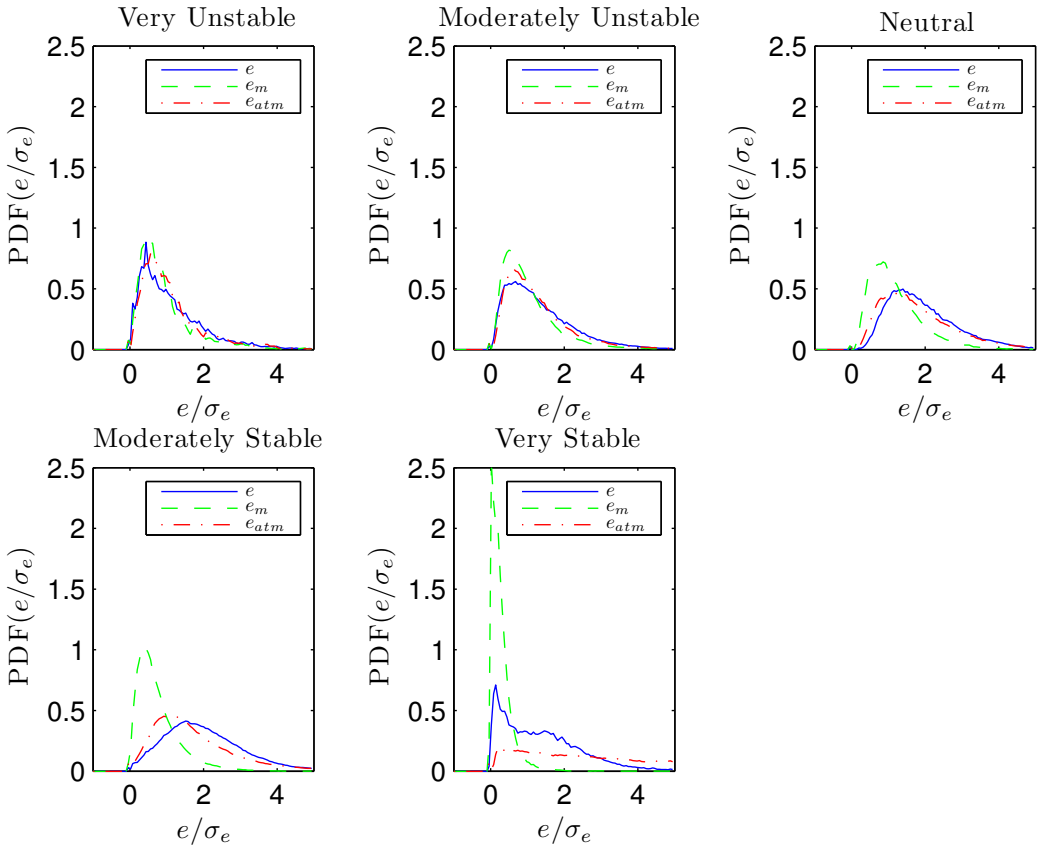

Figure 5.3. PDFs of true and modeled energy for $\Delta/z = 2.0$.

In order to further understand the Δ/z and z/L dependence of the SFS energy models, we calculated the joint PDFs of the true and modeled energy for both models. The joint PDFs are the best measure of the local relationship between the modeled and true energy, since they completely characterize the joint behavior of a pair of random variables. An optimal SFS model would have a joint PDF where the most probable values of e and e_m are found near the 1:1 line with little scatter. The true and modeled energy were normalized by σ_e before calculating a JPDF for each block of data.

The joint PDFs of the true energy and the –5/3 model are given in Figures 5.6, 5.8, and 5.10 for $\Delta/z = 2.0$, 1.0, and 0.5, respectively. For the largest filter

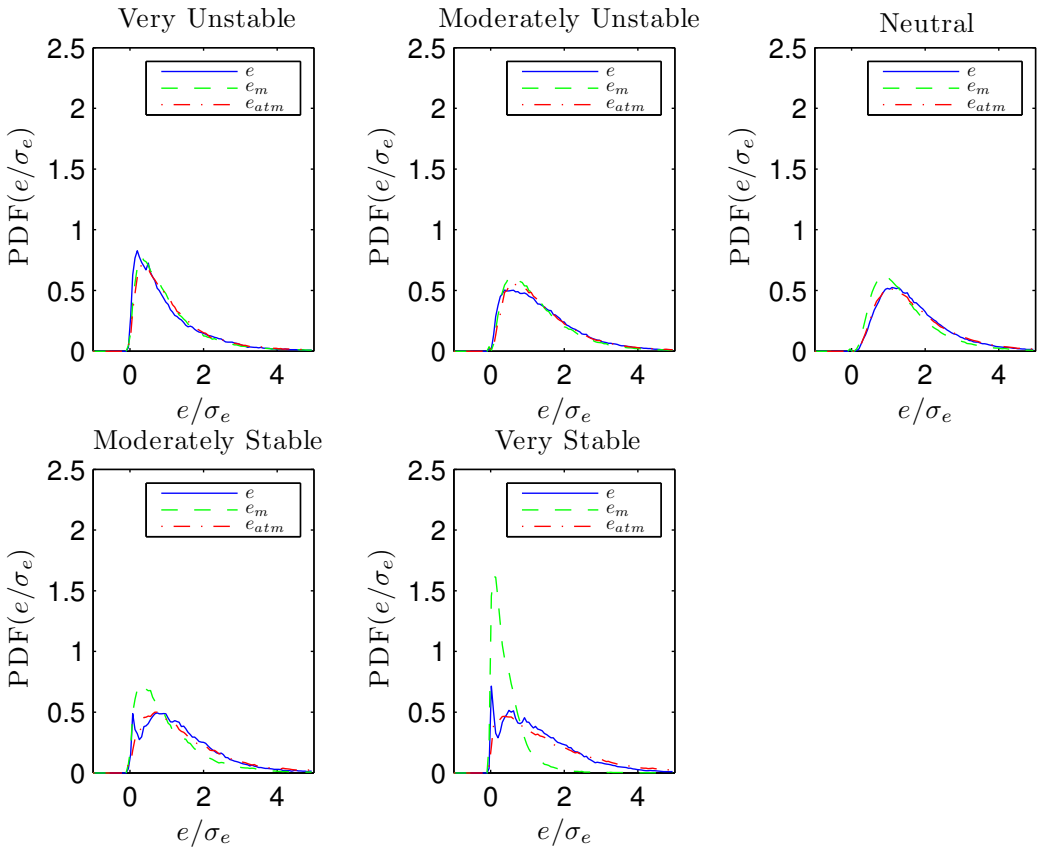

Figure 5.4. PDFs of true and modeled energy for $\Delta/z = 1.0$.

width used in the analysis (Figure 5.6), joint PDFs indicate satisfactory model performance under unstable conditions. The model begins to underpredict the true energy, however, as stability increases.

As the filter width decreases (Figures 5.8 and 5.10), the model prediction improves. The most probable values of e and e_m lie closer to the 1:1 line for neutral and moderately stable data. Model performance for the most stable cases remains poor however, even for $\Delta/z = 0.5$.

The joint PDFs of the true SFS energy and the atmospheric model are presented in Figures 5.7, 5.9, and 5.11. With the exception of the very stable cases, the most probable values of e and e_{atm} remain close to the 1:1 line for all filter widths. Furthermore, the amount of scatter reduces as the filter width decreases. While the predictions of the two models converge for unstable and neutral cases when

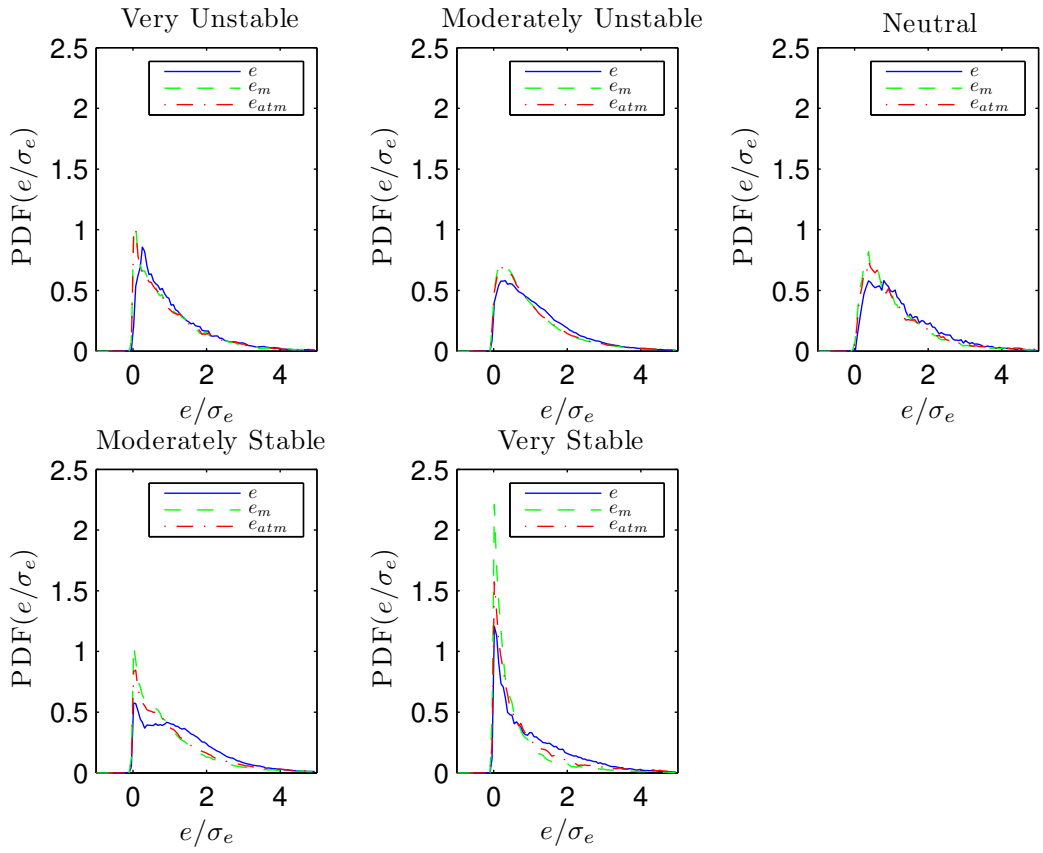

Figure 5.5. PDFs of true and modeled energy for $\Delta/z = 0.5$.

$\Delta/z = 0.5$, the JPDFs indicate that the atmospheric model performs better in stable cases, even for small filter widths.

5.1.3 Discussion of Results

Results from our *a priori* test indicate that our atmospheric SFS energy model produced correct predictions of the average SFS energy under all stabilities and filter widths tested, with the exception of $\Delta/z = 2.0$ for the most stable data. This is an improvement over the –5/3 model, which underpredicts the average energy for large filter widths ($\Delta/z = 2.0$ and 1.0). The atmospheric model remains more accurate under stable conditions than the –5/3 model. We attribute this improvement in model performance to the atmospheric spectral model used to derive our atmospheric SFS energy model. Since the model for $E(z, \kappa)$ represents

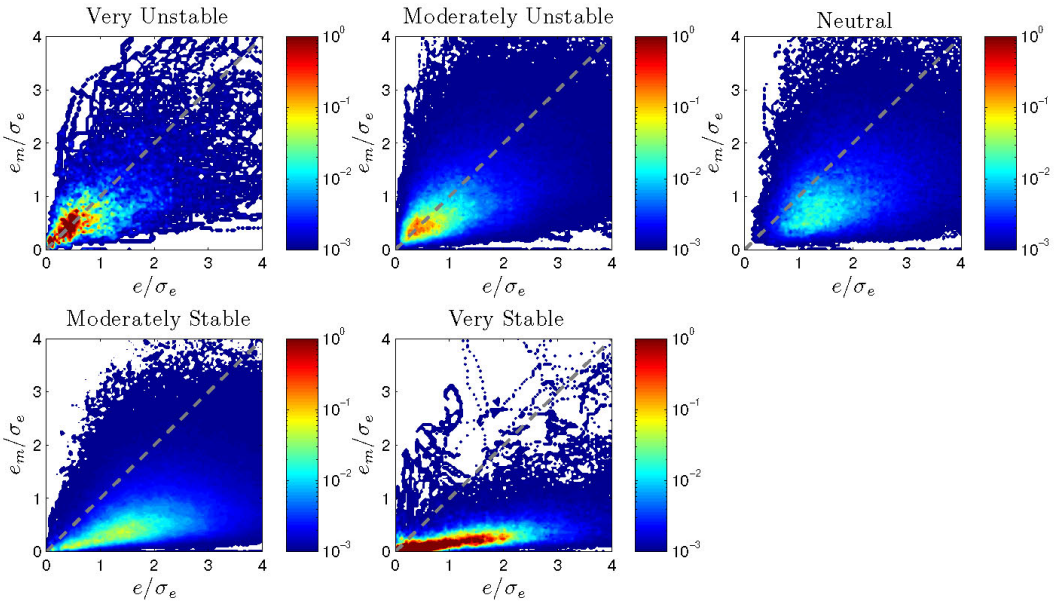

Figure 5.6. Joint PDFs of true SFS energy and –5/3 model, $\Delta/z = 2.0$.

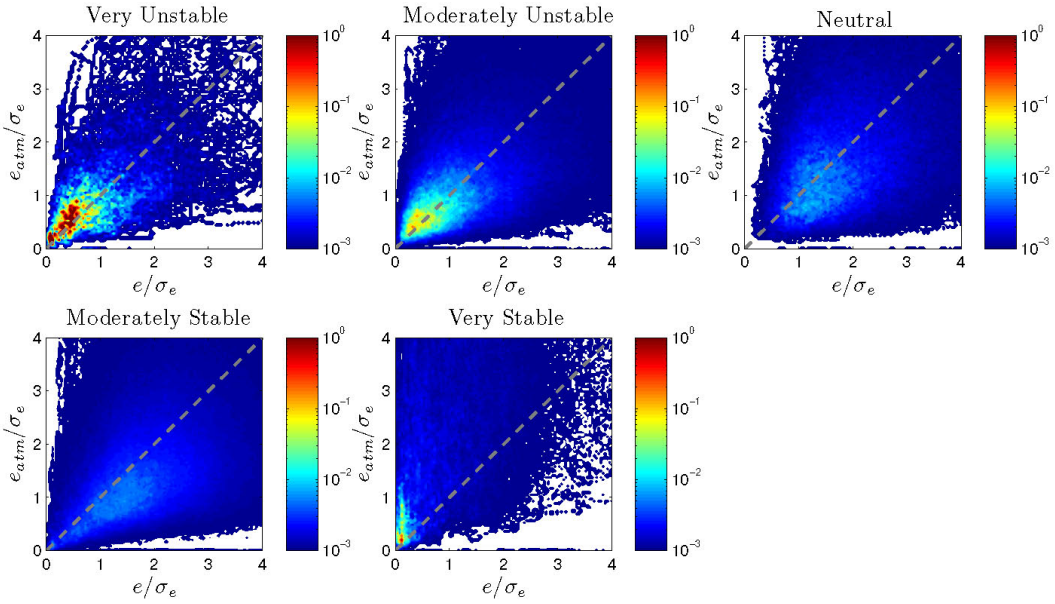

Figure 5.7. Joint PDFs of true SFS energy and atmospheric model, $\Delta/z = 2.0$.

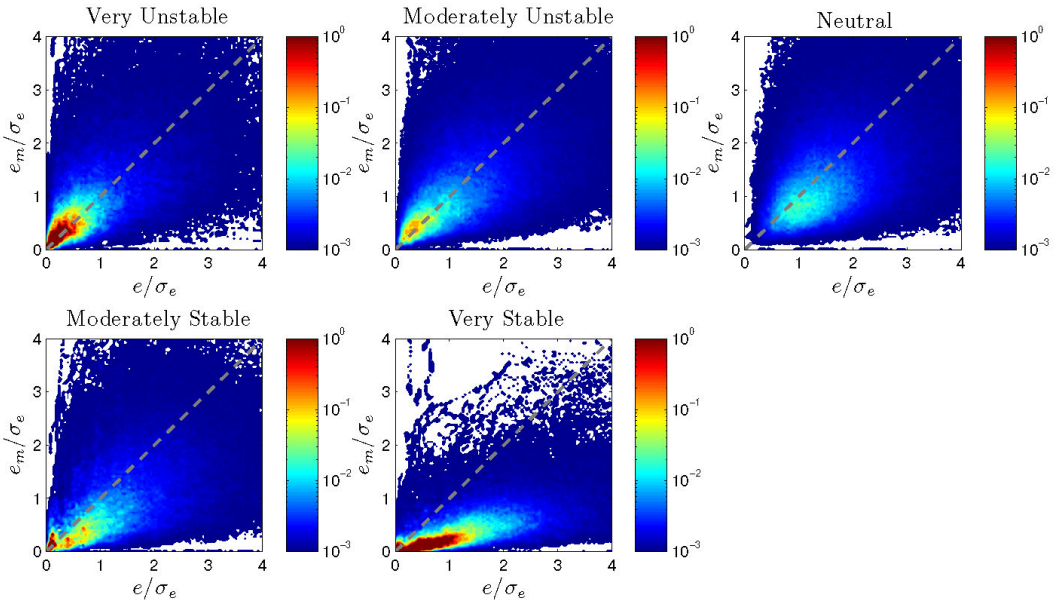

Figure 5.8. Joint PDFs of true SFS energy and –5/3 model, $\Delta/z = 1.0$.

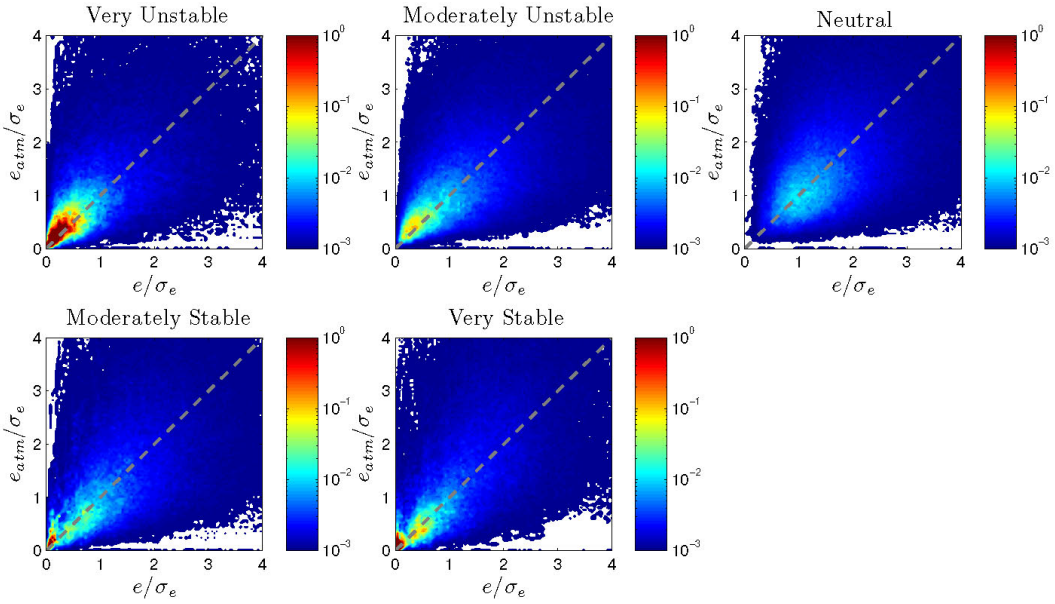

Figure 5.9. Joint PDFs of true SFS energy and atmospheric model, $\Delta/z = 1.0$.

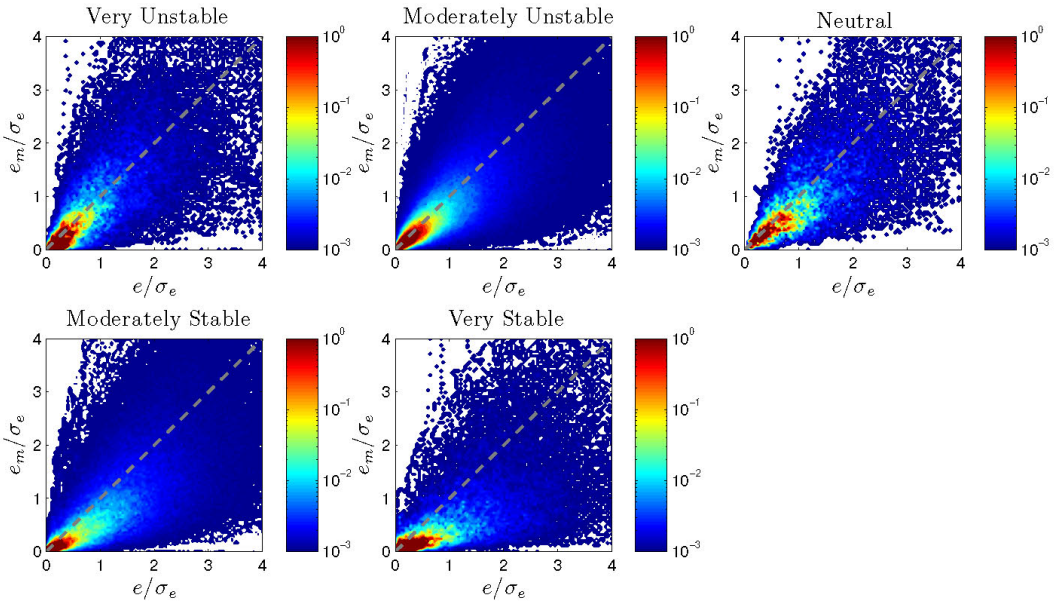

Figure 5.10. Joint PDFs of true SFS energy and –5/3 model, $\Delta/z = 0.5$.

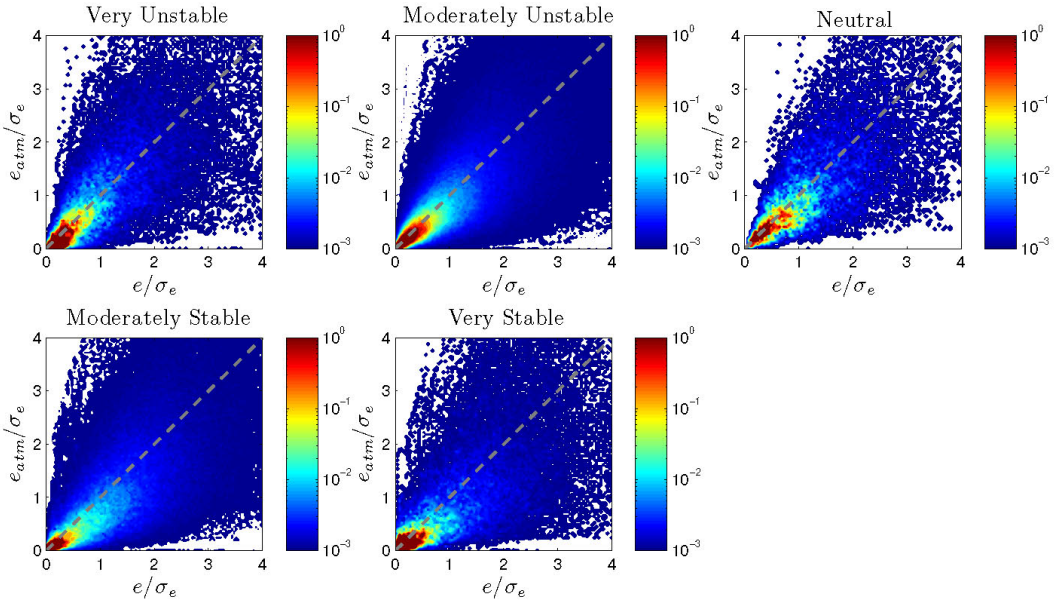

Figure 5.11. Joint PDFs of true SFS energy and atmospheric model, $\Delta/z = 0.5$.

low-wavenumber behavior more accurately than an infinite $\kappa^{-5/3}$ spectrum, the average SFS energy can be predicted correctly even when the single and double filters do not lie in the inertial subrange.

We examined the local performance of the two models through their PDFs and joint PDFs. While both models exhibit similar performance for small filter widths ($\Delta/z = 0.5$), the PDFs predicted by the atmospheric model remain much closer to those of the true energy as filter width increases. Joint PDFs similarly show that the most probable values for the atmospheric model are closer to the 1:1 line than for the –5/3 model, especially under stable stratification.

The atmospheric model exhibited satisfactory local performance under most values of z/L and Δ/z considered, except for very stable runs when $\Delta/z = 2.0$. Therefore, for large filter widths, the performance of the atmospheric model is robust for $-1.0 \leq z/L \leq 0.5$. However, as the filter width decreases, the atmospheric model also performs well under stable conditions. If the filter width is sufficiently small (e.g. $\Delta/z = 0.5$), the –5/3 and atmospheric models have similar performance, because the assumption that both filters lie in the inertial range is met.

5.2 SFS Temperature Variance Model

Another quantity of interest in LES of the ABL, particularly in dispersion modeling, is the SFS scalar variance. The SFS scalar variance must be known if one wishes to estimate the total scalar variance from the resolved scale scalar field; it also is important in some models of the SFS scalar flux. We have chosen to extend our model to the SFS temperature variance, since sonic virtual temperature was measured during HATS. Both a –5/3 model (3.11) and an atmospheric model (3.31) of the SFS temperature variance are derived in §3 using Kolmogorov and atmospheric spectra, respectively. Results from *a priori* tests that assess both global and local model performance are given here.

5.2.1 Global Performance

To quantify the global performance of the –5/3 and atmospheric SFS temperature variance models, the average predicted by each model was calculated for each block of data. Figure 5.12 contains scatterplots of the average values of the models versus $\langle\theta^2_{sfs}\rangle$, the average measured SFS temperature variance; Figure 5.13 is the ratio of the average predicted by the model to $\langle\theta^2_{sfs}\rangle$ plotted as a function of z/L.

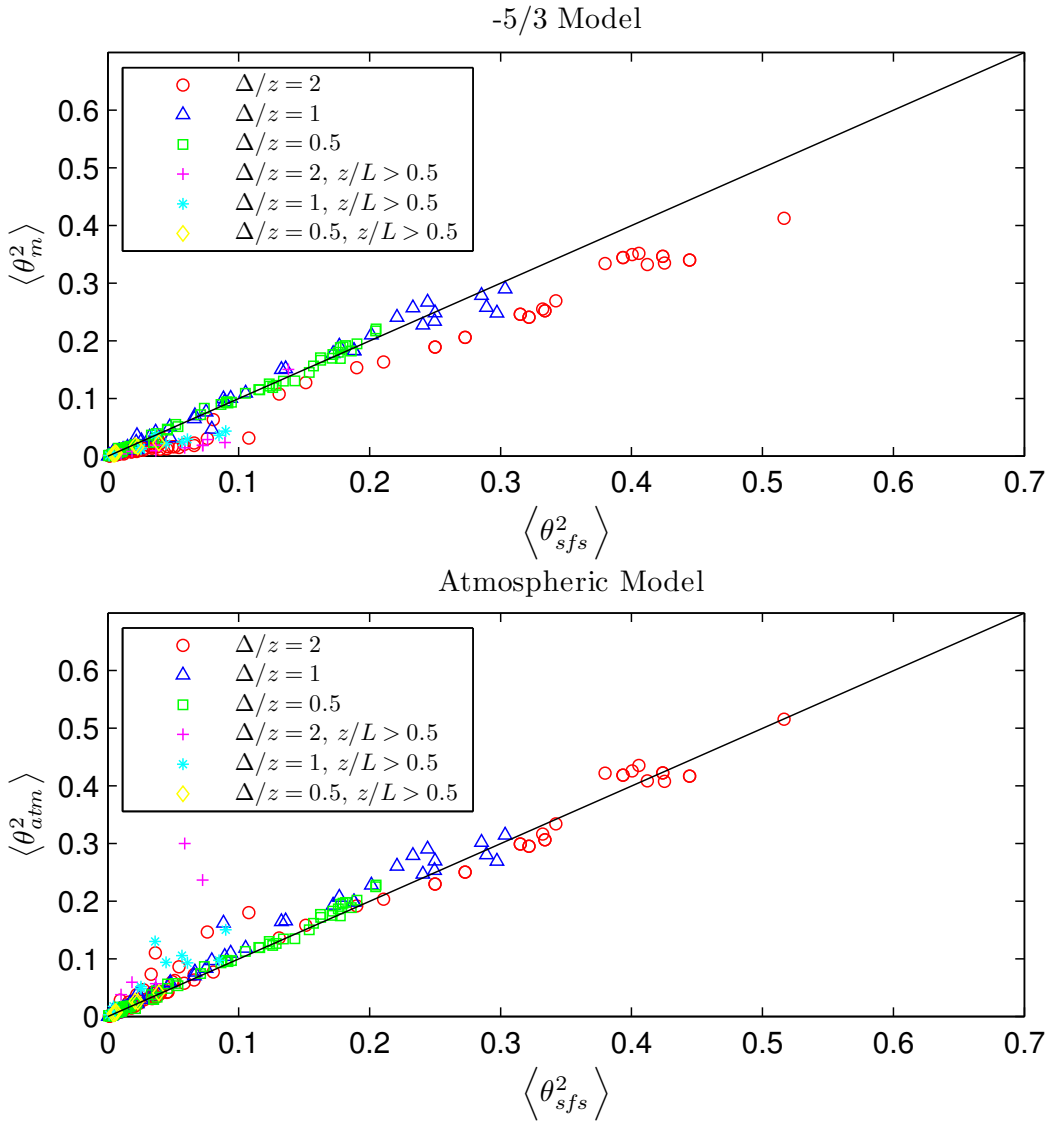

Figure 5.12. Scatterplot of true and modeled SFS temperature variance for each block of data.

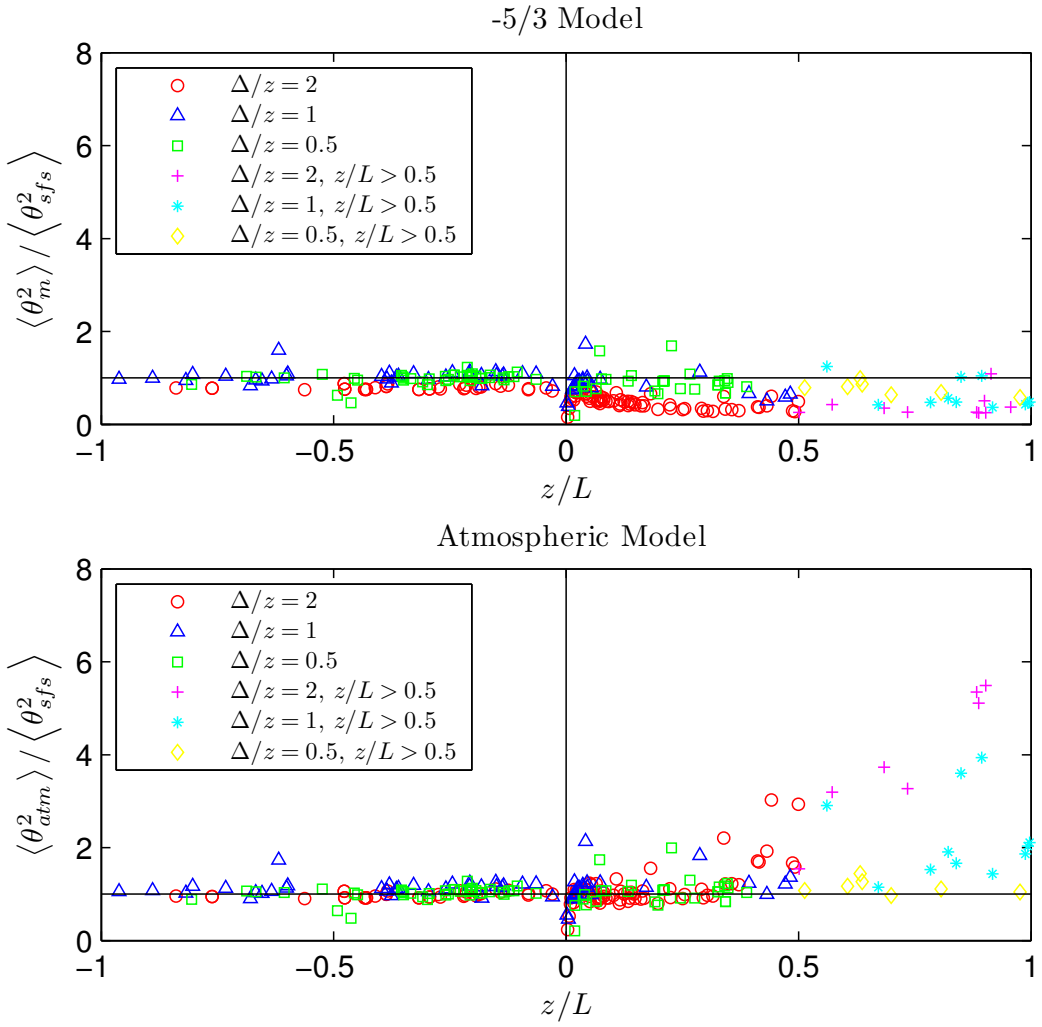

Figure 5.13. Ratio of the averages of the modeled and true SFS temperature variance as a function of z/L.

The models of SFS temperature variance have similar performance to the SFS energy models, although they exhibit more scatter for all filter widths. The atmospheric model predicts $\langle\theta_{sfs}^2\rangle$ more accurately under unstable and neutral conditions than the –5/3 model for $\Delta/z = 2.0$ and 1.0. The predictions of the two temperature variance models converge for a sufficient small filter width ($\Delta/z = 0.5$) as the energy models did.

Figure 5.13 indicates that the –5/3 model underpredicts $\langle\theta_{sfs}^2\rangle$ as stability increases, while the atmospheric model overpredicts $\langle\theta_{sfs}^2\rangle$. For $\Delta/z = 2.0$, the

atmospheric model begins to diverge from a 1:1 prediction of the average near $z/L = 0.4$; this effect occurs at higher stabilities as the filter width decreases. The atmospheric model therefore yields reasonable global predictions of the SFS temperature variance for $-1.0 \leq z/L \leq 0.5$ for all filter widths, which can be extended to slightly more stable conditions for $\Delta/z = 1.0$ or 0.5.

5.2.2 Local Performance

As with the energy, the local performance of the temperature variance models is assessed using PDFs and joint PDFs. Plots of the PDFs for $\Delta/z = 2.0$, 1.0, and 0.5 are given in Figures 5.14–5.16.

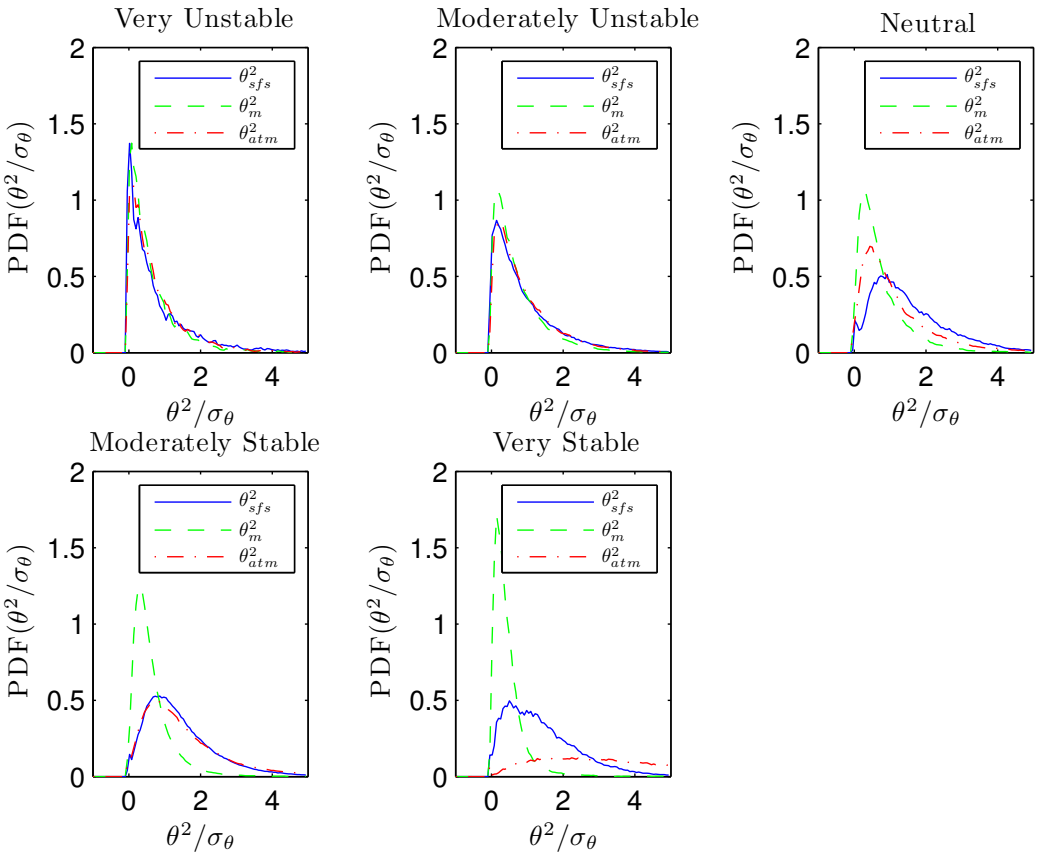

Figure 5.14. PDFs of true and modeled temperature variance for $\Delta/z = 2.0$.

Under unstable conditions, the two models yield similar predictions of the actual SFS temperature variance for all filter widths. Under neutral and moderately

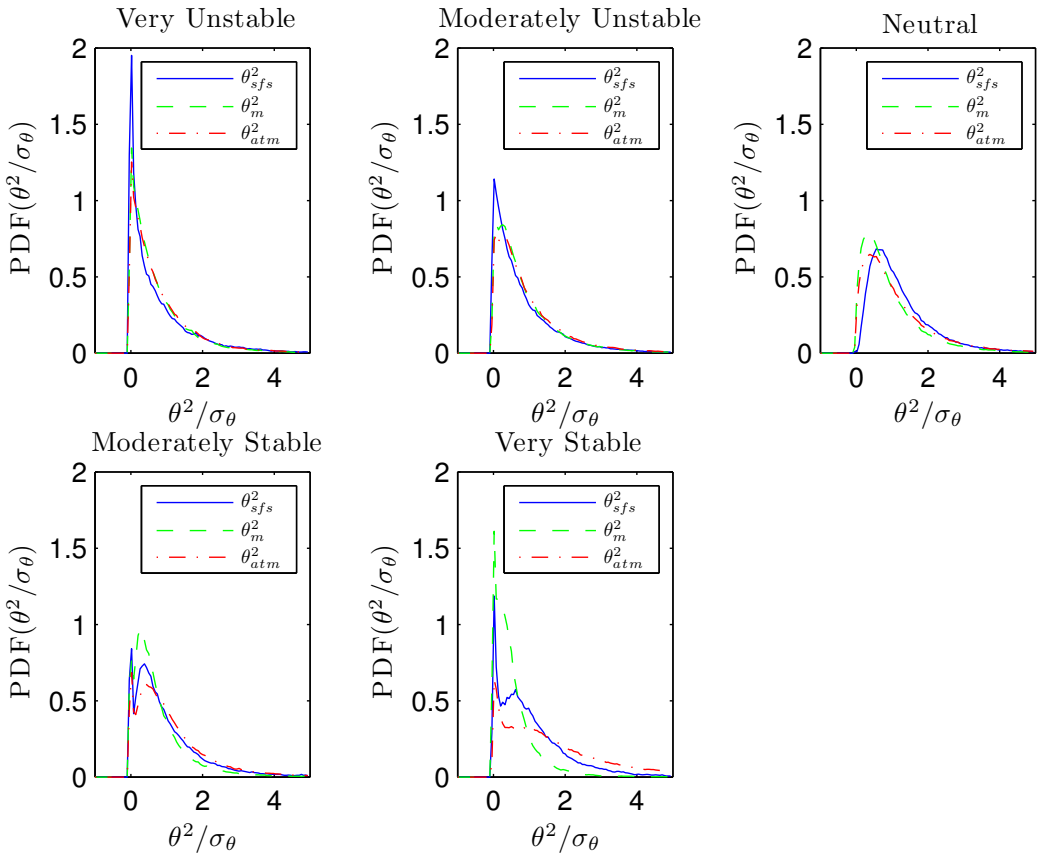

Figure 5.15. PDFs of true and modeled temperature variance for $\Delta/z = 1.0$.

stable conditions when $\Delta/z = 2.0$, the atmospheric model performs better locally than the –5/3 model. Both models have difficulty, however, reproducing the PDF of the true temperature variance under very stable conditions. As the filter width decreases to $\Delta/z = 1.0$, predictions made by the –5/3 model improve; the predictions of the two models converge to the PDF of the true energy for $\Delta/z = 0.5$.

The differences between the predictions of the two models can be seen more clearly in plots of the joint PDFs. JPDFs of the true temperature variance and –5/3 model are displayed in Figures 5.17, 5.19, and 5.21; JPDFs for the true temperature variance and the atmospheric model are given in Figures 5.18, 5.2.2, and 5.22.

For $\Delta/z = 2.0$ data, the –5/3 model consistently overpredicts the correct distribution of θ^2_{sfs} for neutral and stable runs. At this filter width the atmospheric

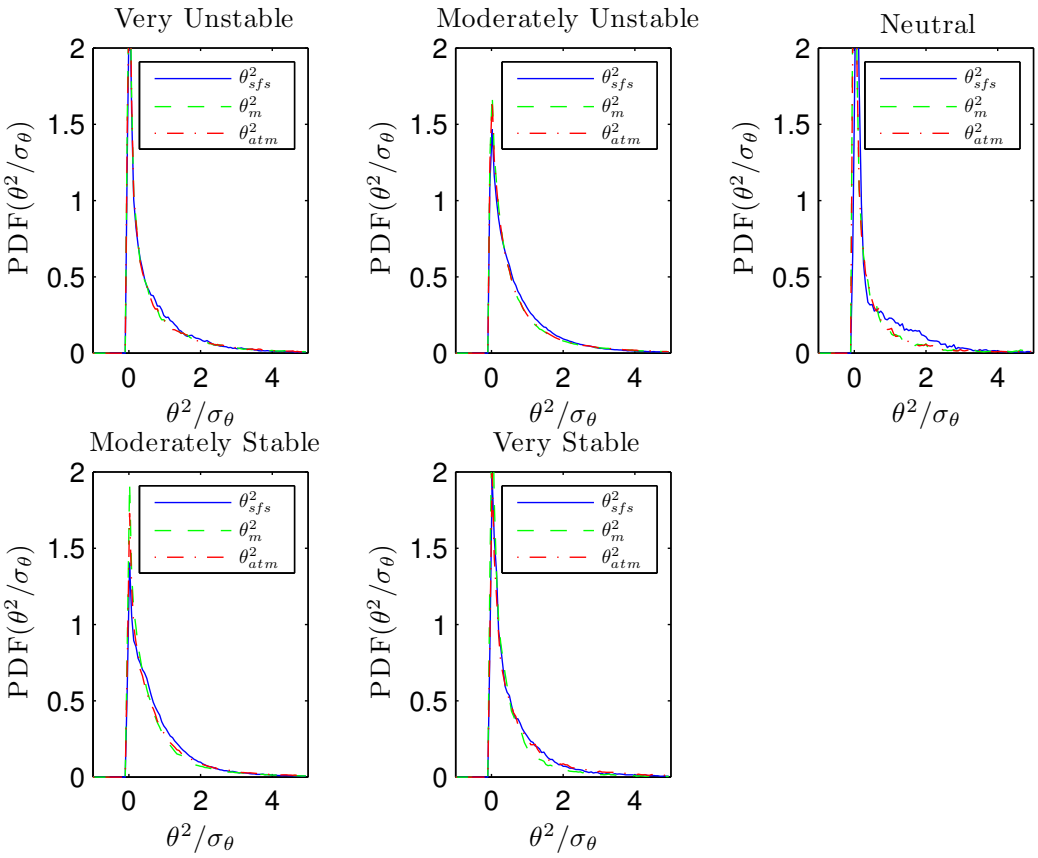

Figure 5.16. PDFs of true and modeled temperature variance for $\Delta/z = 0.5$.

model performs better, except in the very stable case. As Δ/z decreases to 1.0, the atmospheric model still has better performance. The JPDFs again demonstrate that the predictions of the two models converge for $\Delta/z = 0.5$.

5.2.3 Discussion of Results

The overall performance of the atmospheric SFS temperature variance model is slightly worse than that of the atmospheric energy model. From a comparison of spectra calculated from HATS data to the spectral models, it appears that the atmospheric model of the energy spectrum fits the calculated energy spectrum more accurately than the model temperature spectrum fits the calculated temperature spectrum.

If one were using a sufficiently small ratio of filter width to the integral scale

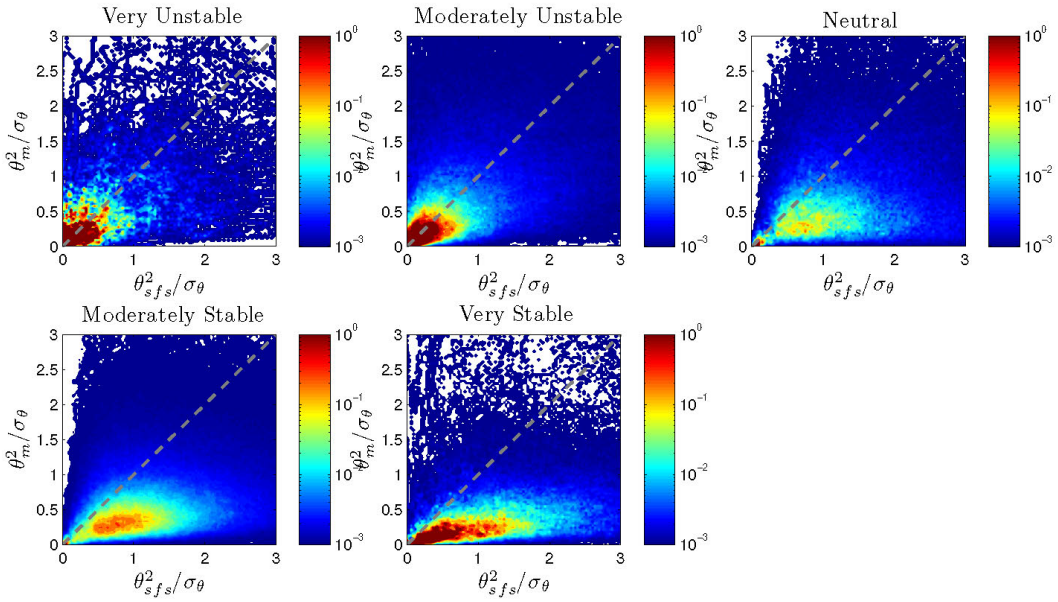

Figure 5.17. JPDFs of true SFS temperature variance and –5/3 model, $\Delta/z = 2.0$.

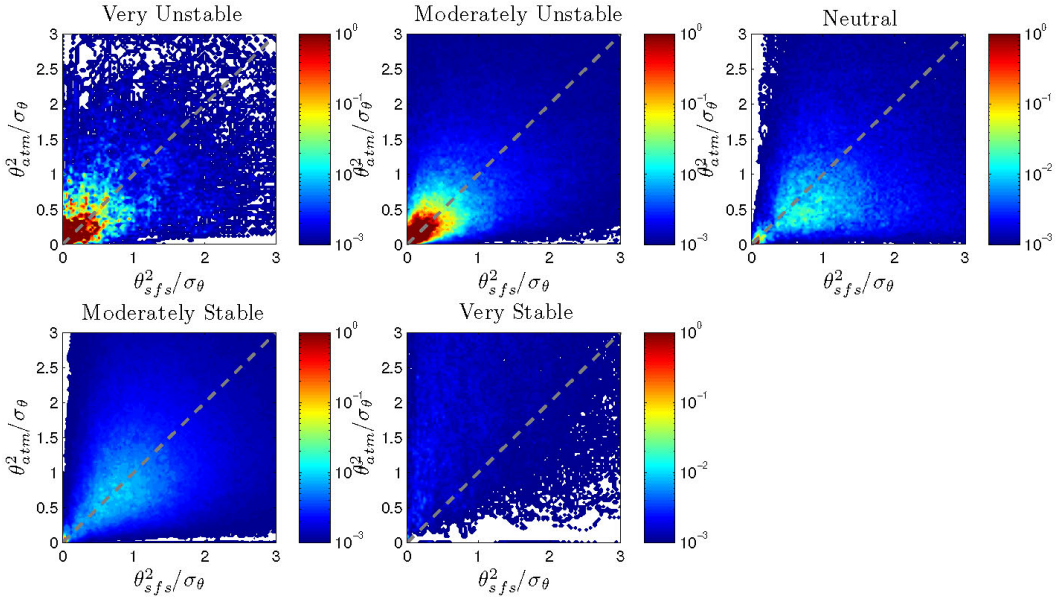

Figure 5.18. JPDFs of true SFS temperature variance and atmospheric model, $\Delta/z = 2.0$.

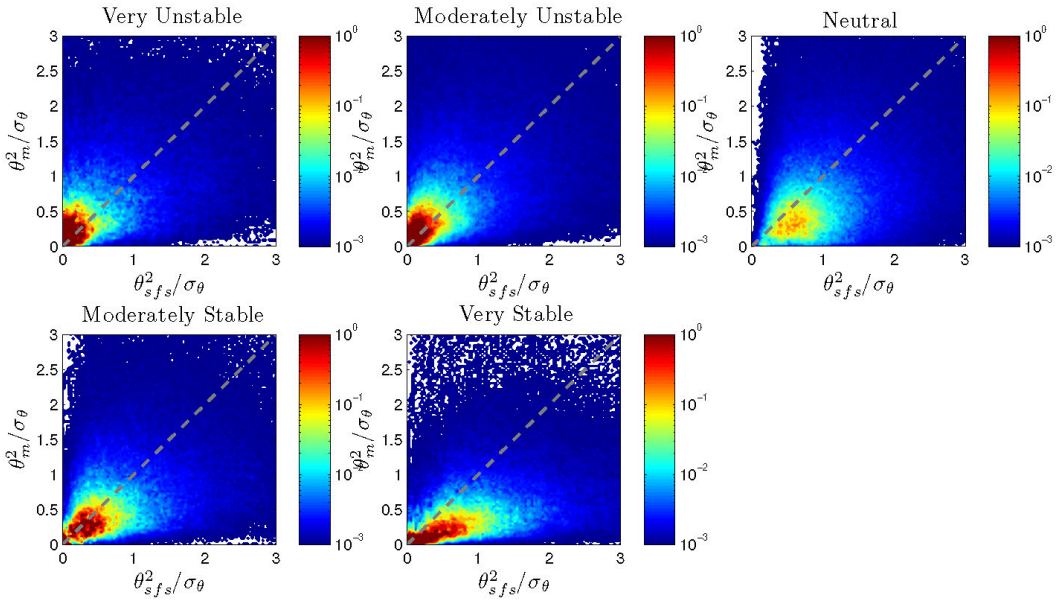

Figure 5.19. JPDFs of true SFS temperature variance and –5/3 model, $\Delta/z = 1.0$.

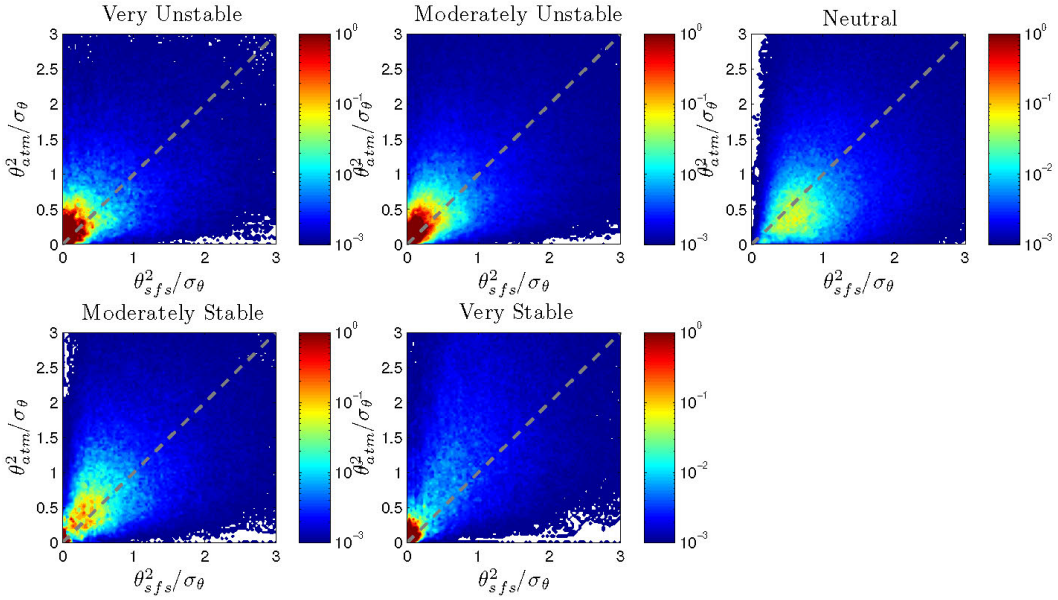

Figure 5.20. JPDFs of true SFS temperature variance and atmospheric model, $\Delta/z = 1.0$.

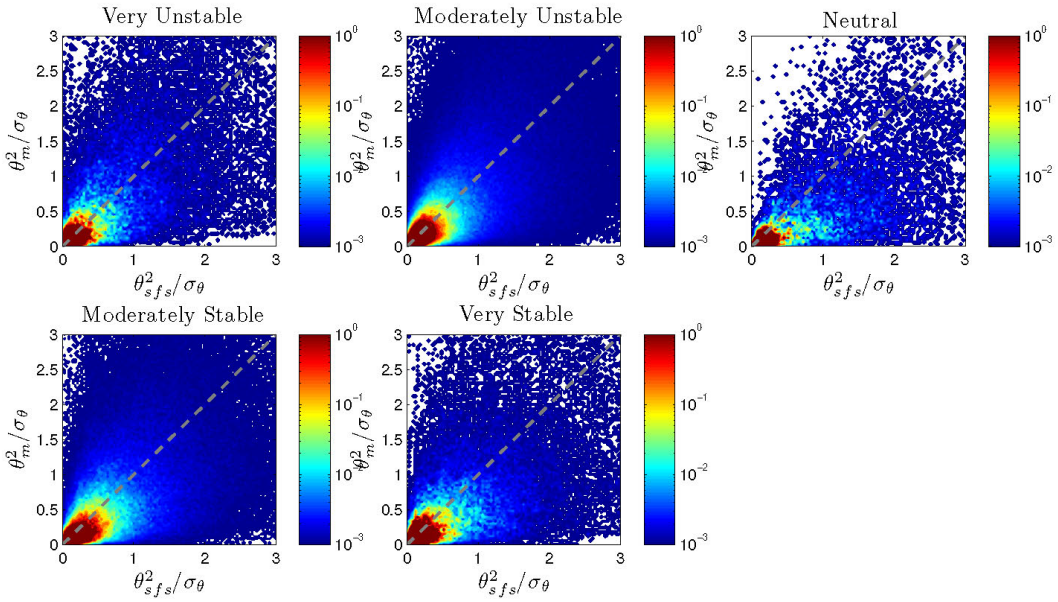

Figure 5.21. JPDFs of true SFS temperature variance and –5/3 model, $\Delta/z = 0.5$.

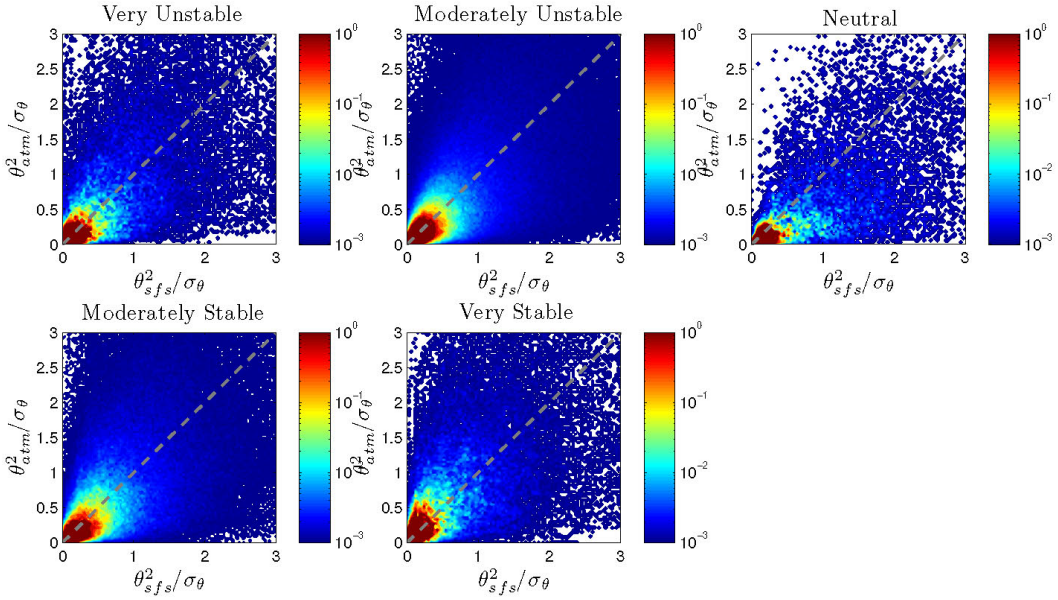

Figure 5.22. JPDFs of true SFS temperature variance and atmospheric model, $\Delta/z = 0.5$.

in LES, use of the atmospheric model would not offer much improvement over the –5/3 model. In the case where both $\widetilde{\Delta}$ and $\bar{\Delta}$ lie in the inertial subrange where $E(\kappa) \sim \kappa^{-5/3}$, the predictions made by the two models will be identical because the all the assumptions made in deriving the –5/3 model are valid in this case. The atmospheric model does have better global and local performance, however, for the large filter widths ($\Delta/z = 2.0$ and 1.0) under unstable and neutral conditions ($-1.0 \leq z/L \leq 0.5$).

5.3 Models for the SFS Velocity Variances

Because the SFS energy has contributions from τ_{11}, τ_{22}, and τ_{33}, an interesting question is whether we can use information from $\langle \widetilde{L}_{ii} \rangle$ and e_{atm} to model the SFS velocity variances (i.e. $\tau_{\alpha\alpha}$, no sum on α). The fraction of the energy contained in each component of $\tau_{\alpha\alpha}^{atm}$ can be taken to be proportional to the ratio between $\langle \widetilde{L}_{\alpha\alpha} \rangle$ and $\langle \widetilde{L}_{ii} \rangle$ via

$$\tau_{\alpha\alpha}^{atm} = 2 \, \frac{\langle \widetilde{L}_{\alpha\alpha} \rangle}{\langle \widetilde{L}_{ii} \rangle} \, e_{atm}. \tag{5.1}$$

Scatterplots of the average values of $\tau_{\alpha\alpha}$ and $\tau_{\alpha\alpha}^{atm}$ are displayed in Figure 5.23 with the scatterplot of the atmospheric model versus true energy also shown for comparison. It is evident from these plots that our model for the diagonal components of τ_{ij} overpredicts the contribution to the SFS energy from τ_{11} and underpredicts the contribution from τ_{33}. While the average is correct for τ_{22}, even this component has more scatter around the 1:1 line than the model of the SFS energy. The performance of the model given in (5.1) improves as Δ/z decreases and as the magnitude of $\langle \tau_{\alpha\alpha} \rangle$ decreases. The stability dependence of this model is evident from Figure 5.24, which gives the ratio between the modeled and true stress as a function of z/L. As was the case with the atmospheric model of the SFS energy, the models for τ_{11} and τ_{22} systematically overpredict the magnitude of the stress for $z/L > 0.5$, although the model of τ_{33} underpredicts the true stress for most values of z/L and Δ/z. These results are not entirely surprising, given that the fraction of the SFS energy contained in each component of $\tau_{\alpha\alpha}$ is determined by the dynamics of the larger scales near $\widetilde{\Delta}$, which are more anisotropic than the scales near $\bar{\Delta}$ when larger filter widths ($\Delta/z = 2.0$, 1.0) are used. This method

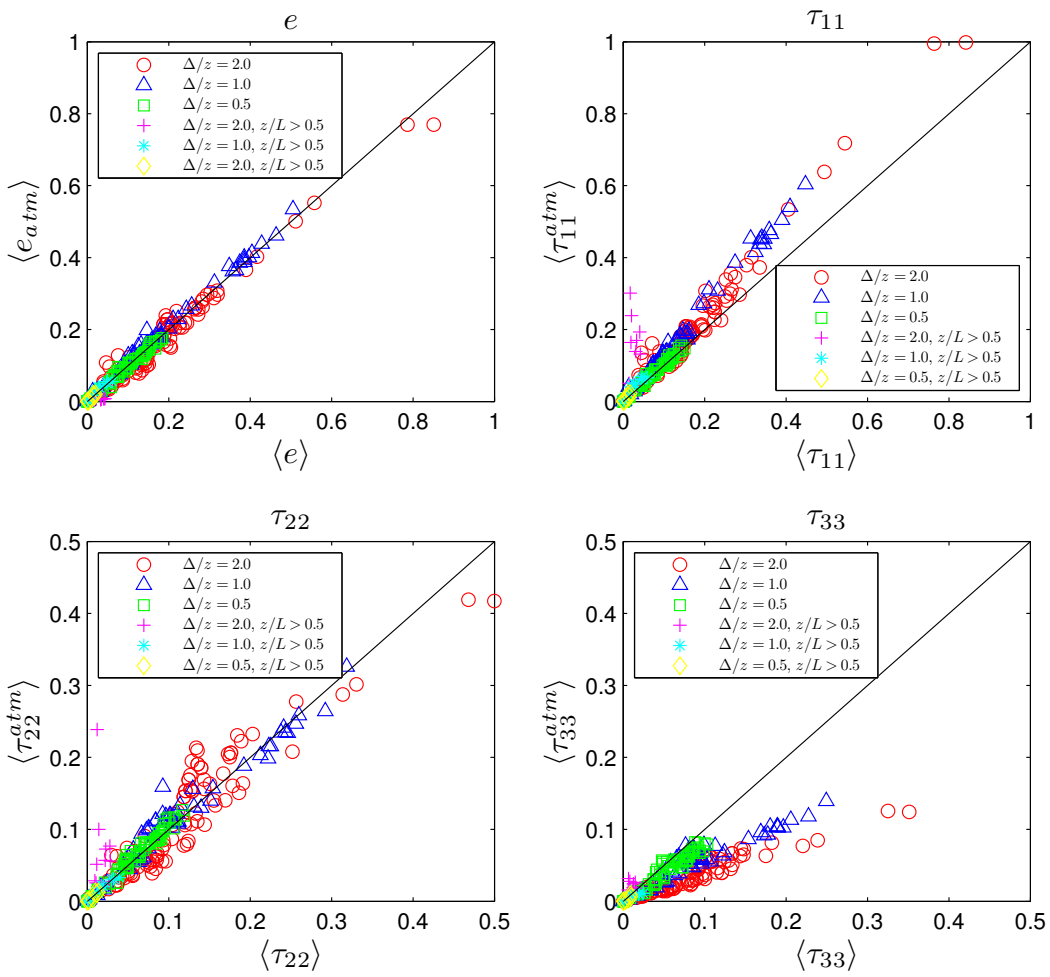

Figure 5.23. Scatterplots of average values of the true and modeled SFS velocity variances. The atmospheric model of the SFS energy is included for reference.

for estimating the SFS component of the velocity variances could be useful if a sufficiently small filter width (i.e. $\Delta/z = 0.5$) was implemented in LES, but does not predict the magnitude of $\tau_{\alpha\alpha}$ correctly for larger filters.

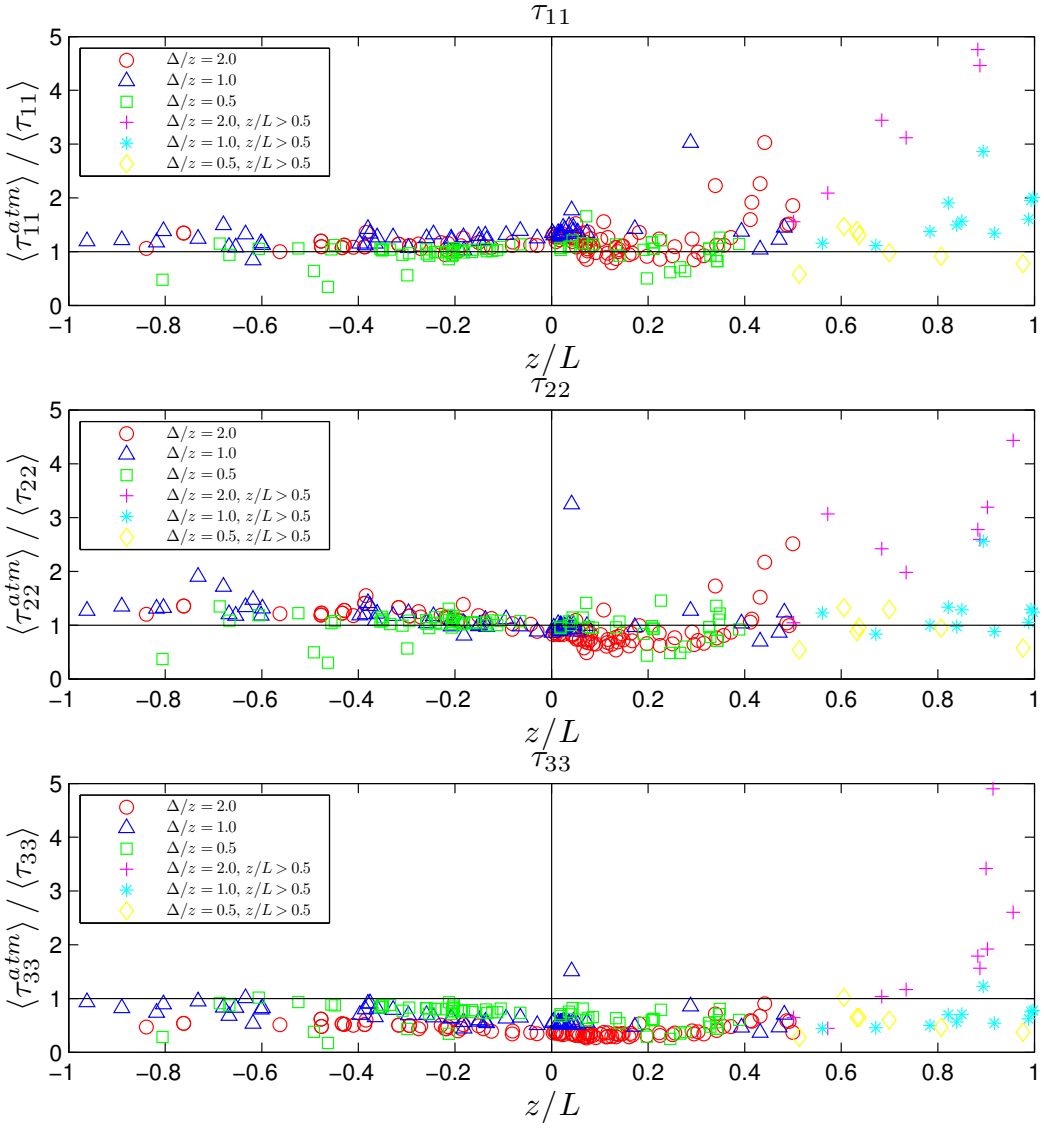

Figure 5.24. Ratios of the modeled to true SFS velocity variances as a function of z/L.

Chapter 6

Summary and Conclusions

The SFS energy is of interest in LES because it can be used to obtain the true pressure field in simulations, to determine a velocity scale for eddy viscosity models of the SFS stress, and to close the equation set in LES when compressibility effects become non-negligible. The common procedure for determining the SFS energy is through the one-equation model, which has a relatively high computational expense and requires closure assumptions for the unknown terms.

A simple model for the SFS energy is proposed that is based on the assumption of scale similarity between τ_{ij} and $\widetilde{L}_{ij}$. The computational expense of our model is low, since $\widetilde{L}_{ij}$ can be calculated easily from information that is available in simulations. Furthermore, the model accounts for atmospheric buoyancy and shear as a function of z/L, the Monin-Obukhov stability parameter.

The performance of the proposed model was assessed in an *a priori* test using atmospheric data from the HATS field experiment. A 2-D Box Filter was used and data was resampled at width Δ to eliminate spurious contributions from small scale information that would not be available in LES. We find that for all values of Δ/z and z/L considered, except for $\Delta/z = 2.0$ and $z/L > 0.5$, the model is able to correctly predict the average SFS energy. For wide filter widths ($\Delta/z = 2.0$ and 1.0) under neutral and stable conditions, the atmospheric model of the energy improves upon a similar model that assumes filtering in the inertial subrange of homogeneous, isotropic turbulence. Since the SFS energy model is derived from a theoretical model of the energy spectrum that accounts for its low wavenumber behavior in the atmosphere, filtering need not occur in the inertial subrange.

The local performance of our model is analyzed through PDFs and joint PDFs. We find that the model is able to reproduce the distribution of the true SFS energy accurately for all conditions except when $\Delta/z = 2.0$ and $z/L > 0.5$ and does so more accurately than the –5/3 model.

We extend these findings to model θ^2_{sfs}, the SFS temperature variance. The performance of the atmospheric and –5/3 models of θ^2_{sfs} is similar for $\Delta/z = 0.5$. However, the atmospheric model improves upon the global and local performance of the –5/3 model for larger filter widths, particularly under neutral and stable conditions. Statistics for the model of θ^2_{sfs} exhibit more scatter than those of the SFS energy, because the model energy spectrum fits the energy spectra calculated from HATS data better than the model temperature spectrum fits the calculated temperature spectra.

A simple procedure was implemented to model the diagonal components of τ_{ij} using information from e_{atm} and $\widetilde{L}_{ij}$. The model overpredicts the magnitude of τ_{11} and underpredicts the magnitude of τ_{33} for $\Delta/z = 2.0$ and 1.0. This result is not surprising, since the fraction of the SFS energy in each component of $\tau_{\alpha\alpha}$ is determined by the ratio $\widetilde{L}_{\alpha\alpha}/\widetilde{L}_{ii}$, and $\widetilde{L}_{ij}$ is more anisotropic than τ_{ij} for large filter widths ($\Delta/z = 2.0$ or 1.0).

Although the SFS energy model that was derived using an atmospheric model for the energy spectrum offers significant improvements over the –5/3 model, the spectral model proposed by Claussen (1985a) scales only with z, and not with the boundary layer depth z_i. Furthermore, the Claussen model does not account for the κ^{-1} behavior of the energy spectrum at low wavenumbers. We expect that a model energy spectrum that includes a κ^{-1} region would lead to a more accurate SFS energy model. While deriving and evaluating a new spectral model is beyond the scope of this current work, the model given by Claussen (1985a) could be modified to include a κ^{-1} region by splitting the inertial subrange into two separate regions and using different timescales for the spectral energy transfer term T_e in each region to replicate both the κ^{-1} and the $\kappa^{-5/3}$ behavior.

Our models for e and θ^2_{sfs} have low computational expense, and are based on information easily attainable in most simulations. Their performance is robust for $-1.0 \leq z/L \leq 0.5$ and $\Delta/z = 2.0$, 1.0, or 0.5. Results of this analysis indicate that the effects of shear and buoyancy can be incorporated into eddy viscosity or

mixed models easily by including a velocity scale based on the atmospheric model of the SFS energy.

Bibliography

Bardina, J., J. Ferziger, and W. Reynolds, 1980: Improved subgrid-scale models for large-eddy simulation. *American Institute of Aeronautics and Astronautics, Fluid and Plasma Dynamics Conference, 13th, Snowmass, Colo., July 14-16, 1980, 10 p.*

Carati, D., S. Ghosal, and P. Moin, 1995: On the representation of backscatter in dynamic localization models. *Physics of Fluids*, **7**, 606.

Chamecki, M., 2010: Modeling subgrid-scale heat fluxes in the neutral and stratified atmospheric boundary layer. *Journal of Turbulence*, **11 (13)**.

Clark, R., J. Ferziger, and W. Reynolds, 1979: Evaluation of subgrid-scale models using an accurately simulated turbulent flow. *Journal of Fluid Mechanics*, **91**, 1–16.

Claussen, M., 1985a: A model of turbulence spectra in the atmospheric surface layer. *Boundary-Layer Meteorology*, **33 (2)**, 151–172.

Claussen, M., 1985b: Estimation of the Monin-Obukhov similarity functions from a spectral model. *Boundary-Layer Meteorology*, **33 (3)**, 233–243.

Cook, A. and J. Riley, 1994: A subgrid model for equilibrium chemistry in turbulent flows. *Physics of Fluids*, **6**, 2868–2870.

Deardorff, J., 1970a: A numerical study of three-dimensional turbulent channel flow at large Reynolds numbers. *Journal of Fluid Mechanics*, **41 (2)**, 453–480.

Deardorff, J., 1970b: Preliminary results from numerical integrations of the unstable planetary boundary layer(Three dimensional numerical model of unstable planetary boundary layer integrated for convecting and turbulent region height, mean lateral shear and Reynolds flux direction). *Journal of the Atmospheric Sciences*, **27**, 1209–1211.

Deardorff, J., 1980: Stratocumulus-capped mixed layers derived from a three-dimensional model. *Boundary-Layer Meteorology*, **18 (4)**, 495–527.

Dias, N. and W. Brutsaert, 1998: Radiative effects on temperature in the stable surface layer. *Boundary-Layer Meteorology*, **89 (1)**, 141–159.

Dyer, A., 1974: A review of flux-profile relationships. *Boundary-Layer Meteorology*, **7 (3)**, 363–372.

Foken, T., 2006: 50 Years of the Monin–Obukhov Similarity Theory. *Boundary-Layer Meteorology*, **119 (3)**, 431–447.

Germano, M., 1986: A proposal for a redefinition of the turbulent stresses in the filtered Navier–Stokes equations. *Physics of Fluids*, **29**, 2323.

Germano, M., U. Piomelli, P. Moin, and W. Cabot, 1991: A dynamic subgrid-scale eddy viscosity model. *Physics of Fluids A: Fluid Dynamics*, **3**, 1760.

Ghosal, S., T. Lund, P. Moin, and K. Akselvoll, 1995: A dynamic localization model for large-eddy simulation of turbulent flows. *Journal of Fluid Mechanics*, **286**, 229–255.

Higgins, C., M. Parlange, and C. Meneveau, 2003: Alignment trends of velocity gradients and subgrid-scale fluxes in the turbulent atmospheric boundary layer. *Boundary-Layer Meteorology*, **109 (1)**, 59–83.

Högström, U., 1988: Non-dimensional wind and temperature profiles in the atmospheric surface layer: A re-evaluation. *Boundary-Layer Meteorology*, **42 (1)**, 55–78.

Horst, T., J. Kleissl, D. Lenschow, C. Meneveau, C. Moeng, M. Parlange, P. Sullivan, and J. Weil, 2004: HATS: Field observations to obtain spatially filtered turbulence fields from crosswind arrays of sonic anemometers in the atmospheric surface layer. *Journal of the Atmospheric Sciences*, **61 (13)**, 1566–1581.

Kaimal, J. and J. Finnigan, 1994: Atmospheric boundary layer flows: Their structure and measurement, 289 pp. Oxford Univ. Press, New York.

Kaimal, J., J. Wyngaard, Y. Izumi, and O. Coté, 1972: Spectral characteristics of surface layer turbulence. *Quarterly Journal of the Royal Meteorological Society*, **98 (417)**, 563–589.

Katul, G., C. Chu, M. Parlange, J. Albertson, and T. Ortenburger, 1995: Low-wavenumber spectral characteristics of velocity and temperature in the atmospheric surface layer. *Journal of Geophysical Research*, **100**, 14–243.

Kleissl, J., C. Meneveau, and M. Parlange, 2003: On the magnitude and variability of subgrid-scale eddy-diffusion coefficients in the atmospheric surface layer. *Journal of the Atmospheric Sciences*, **60 (19)**, 2372–2388.

Kleissl, J., M. Parlange, and C. Meneveau, 2004: Field experimental study of dynamic Smagorinsky models in the atmospheric surface layer. *Journal of the Atmospheric Sciences*, **61 (18)**, 2296–2307.

Knaepen, B., O. Debliquy, and D. Carati, 2002: Subgrid-scale energy and pseudo pressure in large-eddy simulation. *Physics of Fluids*, **14**, 4235.

Leonard, A., 1974: Energy cascade in large-eddy simulations of turbulent fluid flows. *Advances in Geophysics*, **18**, 237–248.

Lilly, D., 1967: The representation of small-scale turbulence in numerical simulation experiments. *Proc. IBM Scientific Computing Symposium on Environmental Sciences*, 195.

Lilly, D., 1992: A proposed modification of the Germano subgrid-scale closure method. *Physics of Fluids A: Fluid Dynamics*, **4**, 633.

Liu, S., C. Meneveau, and J. Katz, 1994: On the properties of similarity subgrid-scale models as deduced from measurements in a turbulent jet. *Journal of Fluid Mechanics*, **275**, 83–119.

Lu, H. and F. Porté-Agel, 2010: A modulated gradient model for large-eddy simulation: Application to a neutral atmospheric boundary layer. *Physics of Fluids*, **22**, 015 109.

Mason, P., 1994: Large-eddy simulation: A critical review of the technique. *Quarterly Journal of the Royal Meteorological Society*, **120 (515)**, 1–26.

McMillan, O. and J. Ferziger, 1979: Direct testing of subgrid-scale models. *AIAA Journal*, **17 (12)**, 1340–1346.

Meneveau, C., 1994: Statistics of turbulence subgrid-scale stresses: Necessary conditions and experimental tests. *Physics of Fluids*, **6 (2)**, 815–833.

Meneveau, C. and J. Katz, 2000: Scale-invariance and turbulence models for large-eddy simulation. *Annual Review of Fluid Mechanics*, **32 (1)**, 1–32.

Meyers, J. and M. Baelmans, 2004: Determination of subfilter energy in large-eddy simulations. *Journal of Turbulence*, **5 (1)**, 26–26.

Misra, A. and D. Pullin, 1997: A vortex-based subgrid stress model for large-eddy simulation. *Physics of Fluids*, **9 (8)**, 2443–2454.

Moeng, C., 1984: A large-eddy-simulation model for the study of planetary boundary-layer turbulence. *Journal of the Atmospheric Sciences*, **41 (13)**, 2052–2062.

Moin, P., K. Squires, W. Cabot, and S. Lee, 1991: A dynamic subgrid-scale model for compressible turbulence and scalar transport. *Physics of Fluids A*, **3 (11)**, 2746–2757.

Pantano, C. and S. Sarkar, 2001: A subgrid model for nonlinear functions of a scalar. *Physics of Fluids*, **13**, 3803–3819.

Pierce, C. and P. Moin, 1998: A dynamic model for subgrid-scale variance and dissipation rate of a conserved scalar. *Physics of Fluids*, **10**, 3041.

Piomelli, U., 1999: Large-eddy simulation: achievements and challenges. *Progress in Aerospace Sciences*, **35 (4)**, 335–362.

Pope, S., 2000: *Turbulent flows*. Cambridge Univ. Press.

Porté-Agel, F., C. Meneveau, and M. Parlange, 1998: Some basic properties of the surrogate subgrid-scale heat flux in the atmospheric boundary layer. *Boundary-Layer Meteorology*, **88 (3)**, 425–444.

Porté-Agel, F., M. Parlange, C. Meneveau, and W. Eichinger, 2001: A priori field study of the subgrid-scale heat fluxes and dissipation in the atmospheric surface layer. *Journal of the Atmospheric Sciences*, **58 (18)**, 2673–2698.

Porté-Agel, F., M. Parlange, C. Meneveau, W. Eichinger, and M. Pahlow, 2000: Subgrid-scale dissipation in the atmospheric surface layer: Effects of stability and filter dimension. *Journal of Hydrometeorology*, **1 (1)**, 75–87.

Pullin, D., 2000: A vortex-based model for the subgrid flux of a passive scalar. *Physics of Fluids*, **12**, 2311.

Sagaut, P., 2006: *Large eddy simulation for incompressible flows: an introduction*. Springer Verlag.

Sarghini, F., U. Piomelli, and E. Balaras, 1999: Scale-similar models for large-eddy simulations. *Physics of Fluids*, **11**, 1596.

Schumann, U., 1975: Subgrid scale model for finite difference simulations of turbulent flows in plane channels and annuli. *Journal of Computational Physics*, **18**, 376–404.

Shaw, R. and U. Schumann, 1992: Large-eddy simulation of turbulent flow above and within a forest. *Boundary-Layer Meteorology*, **61 (1)**, 47–64.

Smagorinsky, J., 1963: General circulation experiments with the primitive equations. *Monthly Weather Review*, **91 (3)**, 99–164.

Sullivan, P., T. Horst, D. Lenschow, C. Moeng, and J. Weil, 2003: Structure of subfilter-scale fluxes in the atmospheric surface layer with application to large-eddy simulation modelling. *Journal of Fluid Mechanics*, **482**, 101–139.

Tong, C., J. Wyngaard, and J. Brasseur, 1999: Experimental study of the subgrid-scale stresses in the atmospheric surface layer. *Journal of the Atmospheric Sciences*, **56 (14)**, 2277–2292.

Voelkl, T., D. Pullin, and D. Chan, 2000: A physical-space version of the stretched-vortex subgrid-stress model for large-eddy simulation. *Physics of Fluids*, **12**, 1810.

Vreman, B., B. Geurts, and H. Kuerten, 1997: Large-eddy simulation of the turbulent mixing layer. *Journal of Fluid Mechanics*, **339**, 357–390.

Wong, V. and D. Lilly, 1994: A comparison of two dynamic subgrid closure methods for turbulent thermal convection. *Physics of Fluids*, **6**, 1016.

Wyngaard, J. and O. Coté, 1971: The budgets of turbulent kinetic energy and temperature variance in the atmospheric surface layer. *Journal of the Atmospheric Sciences*, **28 (2)**, 190–191.

Yoshizawa, A., 1986: Statistical theory for compressible turbulent shear flows, with the application to subgrid modeling. *Physics of Fluids*, **29**, 2152.